Explicit Time Marching Schemes for Solving the Magnetic Field Volume Integral Equation

Sadeed Bin Sayed, *Member, IEEE*, Huseyin Arda Ulku ⓘ, *Senior Member, IEEE*,
and Hakan Bagci ⓘ, *Senior Member, IEEE*

Abstract—A method for constructing explicit marching-on-in-time (MOT) schemes to solve the time-domain magnetic field volume integral equation (TD-MFVIE) on inhomogeneous dielectric scatterers is proposed. The TD-MFVIE is cast in the form of an ordinary differential equation (ODE) and the unknown magnetic field is expanded using curl conforming spatial basis functions. Inserting this expansion into the TD-MFVIE and spatially testing the resulting equation yield an ODE system with a Gram matrix. This system is integrated in time for the unknown time-dependent expansion coefficients using a linear multistep method. The Gram matrix is sparse and well conditioned for Galerkin testing and consists of only four diagonal blocks for point testing. The resulting explicit MOT schemes, which call for the solution of this matrix system at every time step, are more efficient than their implicit counterparts, which call for inversion of a fuller matrix system at lower frequencies. Numerical results compare the efficiency, accuracy, and stability of the explicit MOT schemes and their implicit counterparts for low-frequency excitations. The results show that the explicit MOT scheme with point testing is significantly faster than the other three solvers without sacrificing from accuracy.

Index Terms—Explicit solvers, magnetic field volume integral equation (MFVIE), predictor-corrector scheme, time-domain analysis, transient analysis.

I. INTRODUCTION

ANALYSIS of electromagnetic scattering from inhomogeneous dielectric objects finds applications in numerous areas ranging from medical diagnostics to geophysical surveys. Simulation tools developed for these applications often rely on finite difference time-domain (FDTD) techniques [1]–[4], frequency and time-domain finite element methods (FEMs) [5]–[8], time-domain discontinuous Galerkin (TD-DG) schemes [9]–[13], or frequency and time-domain

volume integral equation (VIE) solvers [14]–[31]. VIE solvers are often preferred over differential equation solvers (such as FDTD, FEM, and TD-DG), for open-region scattering problems, since they require only the scatterer to be discretized and implicitly enforce the radiation condition without the need for (approximate) absorbing boundary conditions to terminate the computation domain [32]. Time-domain VIE (TD-VIE) solvers are preferred over their frequency domain counterparts (FD-VIE solvers) for broadband scattering problems [23]–[31] and/or when the scatterer's permittivity is a (nonlinear) function of the fields [30], [31].

VIEs on dielectric scatterers are constructed by enforcing the fundamental field relation (the total field is equal to the summation of the scattered and incident fields) in the (volumetric) support of the scatterer. The scattered field is represented in terms of the equivalent (unknown) total field/flux induced inside the scatterer. If the electric field is used in the fundamental field relation, then the resulting VIE is termed the electric field VIE (EFVIE) [23]–[31] and the unknown is either the electric flux or the electric field induced inside the scatterer. On the other hand, if the magnetic field is used in the fundamental field relation and the unknown is the total magnetic field, then the magnetic field VIE (MFVIE) is obtained [14].

It is well known that the MFVIE has better convergence characteristics than the EFVIE [16]–[22]. It has also been shown that Galerkin discretization of the EFVIE using Schaubert–Wilton–Glisson (SWG) functions [33] yields a more accurate solution than the MFVIE Galerkin-discretized using the lowest order curl-conforming Nedelec functions [34], [35]. However, this accuracy bottleneck has been circumvented for all practical purposes by using recently developed fully linear curl-conforming (FLC) basis functions to expand the unknown magnetic field [17], [35], [36]. In this case, one can also use point testing, which significantly reduces the computational cost (in comparison to Galerkin testing) without sacrificing from accuracy.

Recent research on FD-VIE solvers has mostly focused on spatial discretization techniques and their effects on the accuracy and conditioning of the resulting matrix systems [14]–[22]. On the other hand, research on TD-VIE solvers has been geared toward developing accurate, efficient, and stable marching-on-in-time (MOT) schemes. TD-VIEs are usually solved using implicit MOT schemes [23]–[26] that call for solution of a matrix system (termed MOT matrix system here) at every time step. These schemes are

not subject to a Courant–Friedrichs–Lewy (CFL) constraint; their time step size is determined only by the maximum frequency of the excitation. For high-frequency excitations, i.e., when the product of the speed of light and the time step size is comparable to the discretization length, the MOT matrix system is sparse and it is solved efficiently using an iterative method. However, for low-frequency excitations, the MOT matrix system becomes fuller and it cannot be solved efficiently using an iterative method.

Depending on the spatial and temporal discretization schemes and the time step size, the MOT scheme can also be explicit. Even though classical explicit MOT schemes do not call for a matrix solution at every time step, they suffer from stability issues [27], [28], which might be remedied using a small time step size at the cost of increased computation time (i.e., they are subject to a CFL constraint).

This article describes a method for constructing explicit MOT schemes, which do not suffer from these shortcomings, to efficiently and accurately solve the TD-MFVIE. The proposed method casts the TD-MFVIE in the form of an ordinary differential equation (ODE) that relates the unknown magnetic field induced inside the scatterer to its temporal derivative [37]. The magnetic field is expanded using the FLC basis functions [35], [36]; inserting this expansion in the TD-MFVIE and spatially testing the resulting equation yields a time-dependent ODE system. A predictor-corrector algorithm, $PE(CE)^m$, is used to integrate this system in time for the unknown coefficients of the expansion. To facilitate the computation of the retarded-time integrals, which express the scattered magnetic field in terms of the unknown magnetic field induced inside the scatterer, at discrete time steps as required by the $PE(CE)^m$, the piecewise Lagrange polynomial interpolation functions [38]–[40] are used. The resulting time marching algorithm calls for the solution of a system with a (spatial) Gram matrix at the evaluation (E) step. When Galerkin testing is used, the Gram matrix is sparse and well conditioned, and the solution is obtained using an iterative solver. When point testing is used, the Gram matrix consists of four diagonal sub-matrices. Its inverse (which also consists of four diagonal sub-matrices) is computed and stored before the time marching starts. Consequently, the matrix solution required at the evaluation step is obtained with a simple multiplication of the right-hand side with the inverse of the Gram matrix. The resulting MOT schemes are expected to be more efficient than their implicit counterparts, which call for the inversion of a matrix system that gets fuller as the time step size gets larger with decreasing frequency. Indeed, the numerical results demonstrate that the explicit MOT schemes use the same time step sizes as the implicit MOT schemes without sacrificing from stability, and they are more efficient under low-frequency excitations. Especially, the explicit MOT scheme with point testing is significantly faster than the other three solvers without sacrificing from accuracy.

The rest of this article is organized as follows: Section II provides the details of the formulation underlying the explicit and implicit MOT schemes with Galerkin and point testing and derives expressions for their computational complexity estimates. Section III compares the efficiency, stability, and accuracy of the explicit MOT schemes and their implicit counterparts for low-frequency excitations via numerical experiments and demonstrates that the explicit scheme with point testing is significantly faster than the other three without sacrificing from accuracy. In Section IV, conclusions and future research directions are drawn.

II. FORMULATION

A. TD-MFVIE

Let V represent the volumetric support of a linear, non-dispersive, non-magnetic, isotropic, and possibly inhomogeneous dielectric scatterer with permittivity $\varepsilon(\mathbf{r})$ and permeability μ_0. The scatterer resides in an unbounded and homogenous medium with permittivity ε_0 and permeability μ_0. An incident magnetic field $\mathbf{H}^{\text{inc}}(\mathbf{r}, t)$, which is essentially band limited to $f_{\max}$ and vanishingly small $\forall \mathbf{r} \in V$ and $t \leq 0$, excites the scatterer. Upon excitation, an equivalent electric current $\mathbf{J}(\mathbf{r}, t)$ is induced inside V, which in return generates a scattered magnetic field $\mathbf{H}^{\text{sca}}(\mathbf{r}, t)$. $\mathbf{H}^{\text{sca}}(\mathbf{r}, t)$ is expressed in terms of retarded-time magnetic vector potential $\mathbf{A}(\mathbf{r}, t)$ as

$$
\begin{aligned}
\mathbf{H}^{\text{sca}}(\mathbf{r}, t) &= \frac{1}{\mu_0} \nabla \times \mathbf{A}(\mathbf{r}, t) \\
&= \nabla \times \int_V \frac{\mathbf{J}(\mathbf{r}', t - R/c_0)}{4\pi R} dv'.
\end{aligned} \tag{1}
$$

Here $R = |\mathbf{r} - \mathbf{r}'|$ is the distance between source point $\mathbf{r}'$ and observation point $\mathbf{r}$, and $c_0 = 1/\sqrt{\varepsilon_0 \mu_0}$ is the speed of light in the background medium. $\mathbf{J}(\mathbf{r}, t)$ is expressed in terms of the total magnetic field $\mathbf{H}(\mathbf{r}, t)$ as

$$
\mathbf{J}(\mathbf{r}, t) = \kappa(\mathbf{r}) \nabla \times \mathbf{H}(\mathbf{r}, t) \tag{2}
$$

where $\kappa(\mathbf{r}) = 1 - \varepsilon_0/\varepsilon(\mathbf{r})$ is the contrast. Substituting (1) and (2) in the temporal derivative of $\mathbf{H}(\mathbf{r}, t) = \mathbf{H}^{\text{inc}}(\mathbf{r}, t) + \mathbf{H}^{\text{sca}}(\mathbf{r}, t)$ yields the TD-MFVIE

$$
\partial_t \mathbf{H}^{\text{inc}}(\mathbf{r}, t) = \partial_t \mathbf{H}(\mathbf{r}, t) + \frac{1}{4\pi} \int_V \kappa(\mathbf{r}') \hat{\mathbf{R}} \tag{3}
$$

$$
\times \left(\frac{\partial_{t'}^2 \nabla' \times \mathbf{H}(\mathbf{r}', t')}{c_0 R} + \frac{\partial_{t'} \nabla' \times \mathbf{H}(\mathbf{r}', t')}{R^2} \right)_{t'=t-R/c_0} dv'
$$

where $\hat{\mathbf{R}} = (\mathbf{r} - \mathbf{r}')/R$.

B. Spatial Basis Functions and Temporal Interpolation

To numerically solve the TD-MFVIE (4), V is divided into a mesh of tetrahedrons. Assume that this mesh has N edges. $\mathbf{H}(\mathbf{r}, t)$ is approximated in terms of the FLC basis functions [35], [36], each of which is defined along one of these edges as

$$
\mathbf{H}(\mathbf{r}, t) = \sum_{n=1}^{N} \{\mathbf{H}^1(t)\}_n \mathbf{f}_n^1(\mathbf{r}) + \sum_{n=1}^{N} \{\mathbf{H}^2(t)\}_n \mathbf{f}_n^2(\mathbf{r}). \tag{4}
$$

Note that this expansion follows the description in [36], where the FLC basis functions are separated into solenoidal and irrotational edge basis functions. In (4), $\mathbf{f}_n^1(\mathbf{r})$ and $\mathbf{f}_n^2(\mathbf{r})$ are the

first-order irrotational edge basis functions [36] and the lowest mixed-order solenoidal edge basis functions [34], and $\{\mathbf{H}^1(t)\}_n$ and $\{\mathbf{H}^2(t)\}_n$ are their unknown time-dependent coefficients, respectively. $\mathbf{f}_n^s(\mathbf{r})$, $s \in \{1, 2\}$ are expressed as

$$\mathbf{f}_n^s(\mathbf{r}) = \begin{cases} \lambda_n^{d_n^1}(\mathbf{r})\nabla\lambda_n^{d_n^2}(\mathbf{r}) \pm \lambda_n^{d_n^2}(\mathbf{r})\nabla\lambda_n^{d_n^1}(\mathbf{r}), & \mathbf{r} \in S_n \\ 0, & \mathbf{r} \notin S_n \end{cases} \quad (5)$$

where "+" and "−" signs should be selected for $s = 1$ and $s = 2$, respectively, $S_n = \cup_{q=1}^{Q_n} S_n^q$ is the combined support of all Q_n tetrahedrons sharing edge n, d_n^1 and d_n^2 represent the two nodes of this edge, and $\lambda_n^d(\mathbf{r})$ and $d \in \{d_n^1, d_n^2\}$ are the barycentric coordinate functions that change linearly from 1 at d to 0 at the face opposite to d. Note that one can easily show $\nabla \times \mathbf{f}_n^1(\mathbf{r}) = 0$ and $\nabla \times \mathbf{f}_n^2(\mathbf{r}) \neq 0$.

To facilitate the discretization and computation of the retarded-time integral in the right-hand side of (4), $\{\mathbf{H}^s(t)\}_n$, $s \in \{1, 2\}$ are approximated using (shifted) Lagrange interpolation functions as

$$\{\mathbf{H}^s(t)\}_n = \sum_{i=1}^{N_t} \{\mathbf{H}_i^s\}_n T(t - i\,\Delta t). \quad (6)$$

Here N_t is the number of time steps, Δt is the time step size, $T(t)$ is a piecewise polynomial Lagrange interpolation function [38]–[40], and $\mathbf{H}_i^s$ is the sample of $\mathbf{H}^s(t)$ at $t = i\,\Delta t$, i.e., $\mathbf{H}_i^s = \mathbf{H}^s(i\,\Delta t)$.

C. Explicit MOT Scheme

Inserting (4) in (4) and testing the resulting equation with functions $\mathbf{t}_m^1(\mathbf{r})$ and $\mathbf{t}_m^2(\mathbf{r})$, $m = 1, \ldots, N$, yield an ODE matrix system of dimension $2N \times 2N$, which relates unknown vectors $\mathbf{H}^s(t)$ to their temporal derivatives $\dot{\mathbf{H}}^s(t) = \partial_t \mathbf{H}^s(t)$, $s \in \{1, 2\}$

$$\begin{bmatrix} \mathbf{G}^{11} & \mathbf{G}^{12} \\ \mathbf{G}^{21} & \mathbf{G}^{22} \end{bmatrix} \begin{bmatrix} \dot{\mathbf{H}}^1(t) \\ \dot{\mathbf{H}}^2(t) \end{bmatrix} = \begin{bmatrix} \dot{\mathbf{H}}^{\text{inc},1}(t) \\ \dot{\mathbf{H}}^{\text{inc},2}(t) \end{bmatrix} + \begin{bmatrix} \dot{\mathbf{H}}^{\text{sca},1}(t) \\ \dot{\mathbf{H}}^{\text{sca},2}(t) \end{bmatrix}. \quad (7)$$

Here $\mathbf{G}^{ps}$, $p, s \in \{1, 2\}$ are $N \times N$ blocks of the Gram matrix $\mathbf{G}$. Their elements are given by

$$\{\mathbf{G}^{ps}\}_{m,n} = \int_{P_m^p} \mathbf{t}_m^p(\mathbf{r}) \cdot \mathbf{f}_n^s(\mathbf{r})dv \quad (8)$$

where P_m^p is the support of $\mathbf{t}_m^p(\mathbf{r})$, $p \in \{1, 2\}$. Two sets of choices are considered for $\mathbf{t}_m^1(\mathbf{r})$ and $\mathbf{t}_m^2(\mathbf{r})$, which result in Galerkin and point testing, respectively. The specific choice of the testing scheme changes the sparseness structure of $\mathbf{G}$ and consequently affects the efficiency and accuracy of the time marching scheme (see Section II-E).

In (7), $\dot{\mathbf{H}}^{\text{inc},p}(t)$ and $\dot{\mathbf{H}}^{\text{sca},p}(t)$, $p \in \{1, 2\}$ are vectors of spatially tested incident and scattered magnetic fields, respectively. Their entries are given by

$$\{\dot{\mathbf{H}}^{\text{inc},p}(t)\}_m = \int_{P_m^p} \mathbf{t}_m^p(\mathbf{r}) \cdot \partial_t \mathbf{H}^{\text{inc}}(\mathbf{r}, t)dv \quad (9)$$

$$\{\dot{\mathbf{H}}^{\text{sca},p}(t)\}_m = \frac{1}{4\pi} \sum_{n=1}^{N} \int_{P_m^p} \mathbf{t}_m^p(\mathbf{r}) \cdot \sum_{q=1}^{Q_n} \kappa_n^q \int_{S_n^q} \hat{\mathbf{R}} \quad (10)$$

$$\times \nabla' \times \mathbf{f}_n^2(\mathbf{r}') \left(\frac{\partial_{t'}^2\{\mathbf{H}^2(t')\}_n}{c_0 R} + \frac{\partial_{t'}\{\mathbf{H}^2(t')\}_n}{R^2} \right)_{t'=t-R/c_0} dv'dv.$$

In (10), $\kappa(\mathbf{r})$ is assumed to be constant in S_n^q, i.e., $\kappa_n^q = \kappa(\mathbf{r}_n^q)$, where $\mathbf{r}_n^q$ is the center of the tetrahedron S_n^q. Also note that since $\nabla \times \mathbf{f}_n^1(\mathbf{r}) = 0$, the only contribution to $\dot{\mathbf{H}}^{\text{sca},p}(t)$ comes from $\nabla \times \mathbf{f}_n^2(\mathbf{r})$.

The samples of the unknown coefficient vectors $\mathbf{H}_j^s = \mathbf{H}^s(j\,\Delta t)$, $s \in \{1, 2\}$ are obtained by integrating the system of ODEs in (7) in time using a PE(CE)^m-type linear k-step scheme. This approach calls for sampling (7) in time

$$\begin{bmatrix} \mathbf{G}^{11} & \mathbf{G}^{21} \\ \mathbf{G}^{12} & \mathbf{G}^{22} \end{bmatrix} \begin{bmatrix} \dot{\mathbf{H}}_j^1 \\ \dot{\mathbf{H}}_j^2 \end{bmatrix} = \begin{bmatrix} \dot{\mathbf{H}}_j^{\text{inc},1} \\ \dot{\mathbf{H}}_j^{\text{inc},2} \end{bmatrix} + \begin{bmatrix} \dot{\mathbf{H}}_j^{\text{sca},1} \\ \dot{\mathbf{H}}_j^{\text{sca},2} \end{bmatrix} \quad (11)$$

where $j = 1, \ldots, N_t$, $\dot{\mathbf{H}}_j^s = \dot{\mathbf{H}}^s(j\,\Delta t)$, $s \in \{1, 2\}$, $\dot{\mathbf{H}}_j^{\text{inc},p} = \dot{\mathbf{H}}^{\text{inc},p}(j\,\Delta t)$, and $\dot{\mathbf{H}}_j^{\text{sca},p} = \dot{\mathbf{H}}^{\text{sca},p}(j\,\Delta t)$, $p \in \{1, 2\}$. $\dot{\mathbf{H}}_j^{\text{inc},p}$ are computed using (9), where $\partial_t \mathbf{H}^{\text{inc}}(\mathbf{r}, t)$ is known. To compute $\dot{\mathbf{H}}_j^{\text{sca},p}$, one has to account for the time retardation in (10); this is done by using temporal interpolation on samples of $\mathbf{H}^2(t)$. Inserting (6) with $s = 2$ in (10) and evaluating the resulting expression at $j\,\Delta t$ yield

$$\dot{\mathbf{H}}_j^{\text{sca},p} = \sum_{i=0}^{j} \mathbf{M}_{j-i}^p \mathbf{H}_i^2, \quad p \in \{1, 2\} \quad (12)$$

where the elements of the MOT matrices $\mathbf{M}_{j-i}^p$ are given by

$$\{\mathbf{M}_{j-i}^p\}_{m,n} = \frac{1}{4\pi} \int_{P_m^p} \mathbf{t}_m^p(\mathbf{r}) \cdot \sum_{q=1}^{Q_n} \kappa_n^q \int_{S_n^q} \hat{\mathbf{R}} \times \nabla' \times \mathbf{f}_n^2(\mathbf{r}')$$

$$\times \left(\frac{\partial_{t'}^2\{T(t')\}_n}{c_0 R} + \frac{\partial_{t'}\{T(t')\}_n}{R^2} \right)_{t'=(j-i)\Delta t - R/c_0} dv'dv. \quad (13)$$

Substituting (12) into (11) yields

$$\underbrace{\begin{bmatrix} \mathbf{G}^{11} & \mathbf{G}^{12} \\ \mathbf{G}^{21} & \mathbf{G}^{22} \end{bmatrix}}_{\mathbf{G}} \underbrace{\begin{bmatrix} \dot{\mathbf{H}}_j^1 \\ \dot{\mathbf{H}}_j^2 \end{bmatrix}}_{\dot{\mathbf{H}}_j} = \underbrace{\begin{bmatrix} \dot{\mathbf{H}}_j^{\text{inc},1} \\ \dot{\mathbf{H}}_j^{\text{inc},2} \end{bmatrix}}_{\dot{\mathbf{H}}_j^{\text{inc}}} + \sum_{i=0}^{j} \underbrace{\begin{bmatrix} \mathbf{0} & \mathbf{M}_{j-i}^1 \\ \mathbf{0} & \mathbf{M}_{j-i}^2 \end{bmatrix}}_{\mathbf{M}_{j-i}^{\text{exp}}} \underbrace{\begin{bmatrix} \mathbf{H}_j^1 \\ \mathbf{H}_j^2 \end{bmatrix}}_{\mathbf{H}_i}. \quad (14)$$

Note that to have a more compact notation, (14) is rewritten as

$$\mathbf{G}\dot{\mathbf{H}}_j = \dot{\mathbf{H}}_j^{\text{inc}} + \sum_{i=0}^{j} \mathbf{M}_{j-i}^{\text{exp}}\mathbf{H}_i. \quad (15)$$

The matrix system (15) is integrated in time using a PE(CE)^m-type linear k-step method (similar to the one used in [37] to solve the time-domain magnetic field surface integral equation). Therefore, it requires the values of $\mathbf{H}_i$ and $\dot{\mathbf{H}}_i$, $i = j - k, \ldots, j - 1$ to compute $\mathbf{H}_j$. Assuming $\mathbf{H}_i$ and $\dot{\mathbf{H}}_i$, $i = 0, \ldots, k - 1$ are known, the steps of the resulting explicit MOT scheme are detailed below.

At each time step, $j = k, \ldots, N_t$.

Step 1: The components of the right-hand side of (15), which are not updated within the time step j, are computed

$$\dot{\mathbf{H}}_j^{\text{fixed}} = \dot{\mathbf{H}}_j^{\text{inc}} + \dot{\mathbf{H}}_j^{\text{exp}} \tag{16}$$

$$= \dot{\mathbf{H}}_j^{\text{inc}} + \sum_{i=0}^{j-1} \mathbf{M}_{j-i}^{\text{exp}} \mathbf{H}_i.$$

Note that $\dot{\mathbf{H}}_j^{\text{exp}}$ does not include the contributions from $\mathbf{H}_j$, i.e., the matrix–vector product $\mathbf{M}_0^{\text{exp}} \mathbf{H}_j$.

Step 2: Predictor (P) step. $\mathbf{H}_j$ is predicted using k past (known) values of $\mathbf{H}_i$ and $\dot{\mathbf{H}}_i$, $i = j-k, \ldots, j-1$, respectively

$$\mathbf{H}_j = \sum_{l=1}^{k} [\{\mathbf{p}\}_l \mathbf{H}_{j-1+l-k} + \{\mathbf{p}\}_{k+l} \dot{\mathbf{H}}_{j-1+l-k}]. \tag{17}$$

Here $\mathbf{p}$ is a vector of dimension $2k$, which stores the predictor coefficients.

Step 3: Evaluation (E) step. First compute the right-hand side using the predicted $\mathbf{H}_j$

$$\mathbf{R}_j = \mathbf{M}_0^{\text{exp}} \mathbf{H}_j + \dot{\mathbf{H}}_j^{\text{fixed}}. \tag{18}$$

Then compute $\dot{\mathbf{H}}_j$ by solving

$$\mathbf{G}\dot{\mathbf{H}}_j = \mathbf{R}_j. \tag{19}$$

Step 4: Set $\dot{\mathbf{H}}_j^{(0)} = \dot{\mathbf{H}}_j$. Repeat Steps 4.1 and 4.2 until convergence ($m = 1, \ldots, m_{\max}$).

    Step 4.1: Corrector (C) step. $\mathbf{H}_j^{(m)}$ corrected/updated using k past values of $\mathbf{H}_i$ and $\dot{\mathbf{H}}_i$, $i = j-k, \ldots, j-1$, and $\dot{\mathbf{H}}_j^{(m-1)}$

$$\mathbf{H}_j^{(m)} = \sum_{l=1}^{k} \left[\{\mathbf{c}\}_l \mathbf{H}_{j-1+l-k} + \{\mathbf{c}\}_{k+l} \dot{\mathbf{H}}_{j-1+l-k} \right]$$

$$+ \{\mathbf{c}\}_{2k+1} \dot{\mathbf{H}}_j^{(m-1)}. \tag{20}$$

Here $\mathbf{c}$ is a vector of dimension $2k+1$, which stores the corrector coefficients.

Step 4.2: Evaluation (E) step. First compute the right-hand side using the corrected $\mathbf{H}_j^{(m)}$

$$\mathbf{R}_j^{(m)} = \mathbf{M}_0^{\text{exp}} \mathbf{H}_j^{(m)} + \dot{\mathbf{H}}_j^{\text{fixed}}. \tag{21}$$

Then compute $\dot{\mathbf{H}}_j^{(m)}$ by solving

$$\mathbf{G}\dot{\mathbf{H}}_j^{(m)} = \mathbf{R}_j^{(m)}. \tag{22}$$

Step 5: Once convergence is reached, solutions are stored to be used at the next time step: $\mathbf{H}_j = \mathbf{H}_j^{(m)}$ and $\dot{\mathbf{H}}_j = \dot{\mathbf{H}}_j^{(m)}$.

The predictor and corrector coefficients, $\mathbf{p}$ and $\mathbf{c}$ used in the above scheme can be obtained by polynomial interpolation between time samples (resulting in well-known schemes such as Adam-Moulton, Adam-Bashfort, or backward difference methods [41]) or numerically under the assumption that the solution can be represented in terms of decaying and oscillating exponentials [42]. In this article, $\mathbf{p}$ and $\mathbf{c}$ obtained through polynomial interpolation are preferred since k associated with these coefficients is much smaller resulting in a more time- and memory-efficient scheme.

At the beginning of time marching, it is assumed that $\mathbf{H}_i = 0$ and $\dot{\mathbf{H}}_i = 0$, $i = 0, \ldots, k-1$. This assumption does not introduce any significant error since $\mathbf{H}^{\text{inc}}(\mathbf{r}, t)$ is vanishingly small $\forall \mathbf{r} \in V$ and $t \leq 0$. For other types of excitations, the Euler method or spectral-deferred correction-type methods can be used to initialize $\mathbf{H}_i$ and $\dot{\mathbf{H}}_i$, $i = 0, \ldots, k-1$ [43], [44].

The method used for solving (19) and (22) is selected based on the sparsity structure of $\mathbf{G}$, which depends on the type of spatial testing used as detailed in Section II-E.

D. Implicit MOT Scheme

Inserting (4) and (6) in (4) and testing the resulting equation with functions $\mathbf{t}_m^1(\mathbf{r})$ and $\mathbf{t}_m^2(\mathbf{r})$, $m = 1, \ldots, N$, yield a linear system of equations

$$\mathbf{M}_0^{\text{imp}} \mathbf{H}_j = \dot{\mathbf{H}}_j^{\text{inc}} - \dot{\mathbf{H}}_j^{\text{imp}}$$

$$= \dot{\mathbf{H}}_j^{\text{inc}} - \sum_{i=0}^{j-1} \mathbf{M}_{j-i}^{\text{imp}} \mathbf{H}_i. \tag{23}$$

Here $\mathbf{H}_j$ and $\dot{\mathbf{H}}_j^{\text{inc}}$ are same as those in (14), and $\mathbf{M}_l^{\text{imp}}$, $l = j - i$ can be expressed in terms of $\mathbf{M}_l^{\text{exp}}$ and $\mathbf{G}$ as

$$\mathbf{M}_l^{\text{imp}} = \mathbf{G}\partial_t T(t)|_{t=l\Delta t} - \mathbf{M}_l^{\text{exp}}$$

$$= \begin{bmatrix} \mathbf{G}^{11} \ \partial_t T(t)|_{t=l\Delta t} & \mathbf{G}^{12} \ \partial_t T(t)|_{t=l\Delta t} - \mathbf{M}_l^1 \\ \mathbf{G}^{21} \ \partial_t T(t)|_{t=l\Delta t} & \mathbf{G}^{22} \ \partial_t T(t)|_{t=l\Delta t} - \mathbf{M}_l^1 \end{bmatrix}. \tag{24}$$

The implicit MOT scheme operates as briefly described next. For $j = 1$, $\mathbf{H}_1$ is found by solving (23) with right-hand side $\dot{\mathbf{H}}_1^{\text{inc}}$. For $j = 2$, $\mathbf{H}_1$ is used to compute the matrix–vector product $\mathbf{M}_1^{\text{imp}} \mathbf{H}_1$, which is subtracted from $\dot{\mathbf{H}}_2^{\text{inc}}$ to yield the complete right-hand side. $\mathbf{H}_2$ is found by solving (23) with this right-hand side. For $j = 3$, $\mathbf{H}_1$ and $\mathbf{H}_2$ are used to compute the summation $\mathbf{M}_2^{\text{imp}} \mathbf{H}_1 + \mathbf{M}_1^{\text{imp}} \mathbf{H}_2$, which is subtracted from $\dot{\mathbf{H}}_3^{\text{inc}}$ to yield the complete right-hand side. This permits the computation of $\mathbf{H}_3$ and so on.

Unlike the explicit MOT scheme, the method used for solving (23) at every time step of the implicit MOT scheme does not depend on the sparsity structure of $\mathbf{G}$. The solution of this matrix equation is always obtained using an iterative solver.

E. Spatial Testing Functions

Two different approaches are used to spatially test the TD-MFVIE: Point and Galerkin testing schemes [36]. The choice of testing functions $\mathbf{t}_m^p(\mathbf{r})$, $p \in \{1, 2\}$, changes the sparsity structure of $\mathbf{G}$ in (8) as explained next.

1) Point Testing: For point testing, $\mathbf{t}_m^p(\mathbf{r}) = \hat{\mathbf{q}}_m \delta(\mathbf{r} - \mathbf{r}_m^p)$, $p \in \{1, 2\}$, where $\hat{\mathbf{q}}_m$ is a unit vector that points from node d_m^1 to d_m^2 (along edge m) and $\mathbf{r}_m^p$ are selected from Gaussian quadrature points defined on edge m. Inserting the expressions for $\mathbf{t}_m^p(\mathbf{r})$ into (8) and using the facts that, on edge n, the tangential component of $\mathbf{f}_n^1(\mathbf{r})$ linearly increases from -1 to 1 and the tangential component of $\mathbf{f}_n^2(\mathbf{r})$ stays constant at 1, yield

$$\mathbf{G}^{12} = \mathbf{G}^{22} = \mathbf{I}$$
$$\mathbf{G}^{11} = -\mathbf{G}^{21} = -\frac{1}{\sqrt{3}}\mathbf{I}. \tag{25}$$

The inverse of $\mathbf{G}$ can be expressed as

$$\mathbf{G}^{-1} = \frac{1}{2}\begin{bmatrix} \mathbf{I} & \mathbf{I} \\ \sqrt{3}\mathbf{I} & -\sqrt{3}\mathbf{I} \end{bmatrix}. \tag{26}$$

$\mathbf{G}^{-1}$ is stored using $O(N)$ memory before the time marching starts. Using the pre-computed $\mathbf{G}^{-1}$, the solution of (19) and (22) is obtained only in $O(N)$ operations. This makes the explicit MOT scheme with point testing significantly faster than the other explicit and implicit MOT schemes under low-frequency excitations (for large Δt) as shown by the computational complexity analysis carried out in Section II-G (as also demonstrated by the numerical results presented in Section III).

2) Galerkin Testing: For Galerkin testing, $\mathbf{t}_m^1(\mathbf{r}) = \mathbf{f}_m^1(\mathbf{r})$ and $\mathbf{t}_m^2(\mathbf{r}) = \mathbf{f}_m^2(\mathbf{r})$. Inserting the expressions for $\mathbf{t}_m^p(\mathbf{r})$ into (8), one obtains a summation of integrals, each of which has a second-order polynomial integrand defined over a tetrahedron. These integrals are evaluated exactly using a Gaussian quadrature rule specifically designed for tetrahedrons [45], [46]. Analytical expressions can be derived for these integrals but evaluating those would be more computationally expensive than using a quadrature rule.

When Galerkin testing is used, $\mathbf{G}$ is sparse and well conditioned regardless of Δt. Therefore the solution of (19) and (22) is obtained very efficiently using an iterative scheme. The resulting MOT scheme with Galerkin testing is faster than its implicit counterpart under low-frequency excitations (for large Δt). This is because $\mathbf{M}_0^1$ and $\mathbf{M}_0^2$ become fuller (see Section II-F) as Δt increases and the computational cost of solving (23) increases. Implicit and explicit schemes have similar computational costs under high-frequency excitations (for small Δt). These are shown by the computational complexity analysis carried out in Section II-G (also by the numerical results presented in Section III).

F. Comments

Several comments about the formulation and implementation of the explicit and implicit MOT schemes are in order.

1) In (4), temporal derivative form of $\mathbf{H}(\mathbf{r}, t) = \mathbf{H}^{\mathrm{inc}}(\mathbf{r}, t) + \mathbf{H}^{\mathrm{sca}}(\mathbf{r}, t)$ is used. This additional derivate is needed to cast the TD-MFVIE in the form of an ODE. In this form, the derivative of the unknown $\partial_t \mathbf{H}(\mathbf{r}, t)$ has to be set equal to a function of $\mathbf{H}(\mathbf{r}, t)$. Here this function is $\partial_t \mathbf{H}^{\mathrm{inc}}(\mathbf{r}, t) + \partial_t \mathbf{H}^{\mathrm{sca}}(\mathbf{r}, t)$ and is integrated in time by the explicit MOT scheme to yield $\mathbf{H}(\mathbf{r}, t)$. The effect of the additional temporal derivative has been studied in the context of the MOT solution of the time-domain electric field surface integral equation [47]. When the derivative of a time-domain integral equation is solved by an MOT scheme, a dc component is often observed in the solution even if the zero initial condition is enforced at the beginning of time marching. The reason for this dc component is attributed to numerical errors, especially those arising from the solution of the

MOT matrix system as discussed in [47]. The numerical results presented in Section III-B demonstrate that a similar discussion applies in the case of the MOT schemes developed in this article to solve (4). The results show that the dc component is stable with a small amplitude, and this amplitude can be reduced by increasing the accuracy of the matrix solution and/or correction updates.

2) Temporal interpolation function $T(t)$ is discretely causal: $T(t) = 0$ for $t \le -\Delta t$. This means that, during time marching (as executed by both the explicit and implicit MOT schemes), $\mathbf{H}_i$, $i > j$ ["future" samples of $\mathbf{H}(t)$] are not required to compute $\mathbf{H}_j$. Additionally, $T(t)$ is of finite duration: $T(t) = 0$ for $t > t_{\max}\Delta t$, where $t_{\max}$ is the order of the polynomial interpolation. Note that $T(t)$ can be a noncausal interpolation function. For example, one can use the approximate prolate spheroidal wave functions (APSWFs) [48], [49] since they can interpolate band-limited functions with exponentially increasing accuracy and they have continuous derivatives everywhere along their support. A non causal $T(t)$ means that $\mathbf{M}_{j-i}^p \ne \mathbf{0}$, $i > j$ and consequently the time marching requires $\mathbf{H}_i$, $i > j$ to be able to compute $\mathbf{H}_j$. The causality of the time marching can be restored using various extrapolation schemes that estimate $\mathbf{H}_i$, $i > j$ using $\mathbf{H}_i$, $i \le j$ [26], [49].

3) The MOT matrices $\mathbf{M}_{j-i}^p = \mathbf{0}$ for $j - i > D_{\max}/(c_0 \Delta t) + t_{\max}$, where $D_{\max}$ is the maximum distance between any two points in V. Consequently, as Δt increases (for low-frequency excitations), the number of nonzero $\mathbf{M}_{j-i}^p$ decreases. However, these nonzero matrices become fuller. For example, for $\mathbf{M}_{j-i}^p$ to be completely full, $t_{\max} > j - i > D_{\max}/(c_0 \Delta t) - 1$, which can only be satisfied when $D_{\max} < c_0 \Delta t$ since $j \geqslant i$.

4) A closer look at (24) reveals that $\mathbf{G}$ contributes to $\mathbf{M}_l^{\mathrm{imp}}$ only when its entries are nonzero [see (8)] and when $\partial_t T(t)|_{t=l\Delta t} \ne 0$. Note that the second condition is satisfied only for $l \in \{0, 1, \ldots, t_{\max}\}$. Addition of $\mathbf{G}^{12}$ and $\mathbf{G}^{22}$ to $\mathbf{M}_0^1$ and $\mathbf{M}_0^2$, respectively, does not affect the sparsity structure of $\mathbf{M}_0^{\mathrm{imp}}$. On the other hand, inclusion of $\mathbf{G}^{11}$ and $\mathbf{G}^{21}$ in $\mathbf{M}_0^{\mathrm{imp}}$ reduces its sparsity level; however, this difference can be ignored in the computational complexity analysis as Δt gets larger for low-frequency excitations since $\mathbf{M}_0^1$ and $\mathbf{M}_0^2$ become fuller while $\mathbf{G}^{11}$ and $\mathbf{G}^{21}$ stay sparse.

Note that inclusion of $\mathbf{G}^{11}$ and $\mathbf{G}^{21}$ in $\mathbf{M}_{j-i}^{\mathrm{imp}}$ makes the cost of computing $\dot{\mathbf{H}}_j^{\mathrm{imp}}$ [see (24)] higher than that of $\dot{\mathbf{H}}_j^{\mathrm{exp}}$ [see (16)]. However, since $t_{\max} \ll D_{\max}/(c_0 \Delta t)$ for small Δt (under high-frequency excitations) and $\mathbf{G}^{11}$ and $\mathbf{G}^{21}$ are sparser than $\mathbf{M}_{j-i}^1$ and $\mathbf{M}_{j-i}^2$ for large Δt (under low-frequency excitations), this difference can be ignored in the computational complexity analysis.

G. Computational Complexity

In this section, computational complexity of the explicit MOT scheme described in Section II-C is analyzed in detail

and compared to that of its implicit counterpart described in Section II-D. Let the computational costs of explicit schemes with point and Galerkin testing and the implicit scheme be represented by $C_{\mathrm{PT}}^{\exp} N_{\mathrm{t}} + C$, $C_{\mathrm{GT}}^{\exp} N_{\mathrm{t}} + C$, and $C^{\mathrm{imp}} N_{\mathrm{t}} + C$, respectively. Note that the implicit MOT scheme can also be implemented using Galerkin or point testing, but the expressions for these implementations' computational complexity would be the same. That is why C^{imp} does not distinguish between these two implementations.

Here C represents the total cost of computing $\dot{\mathbf{H}}_j^{\mathrm{fixed}}$ for all time steps $j = 1, \ldots, N_{\mathrm{t}}$ and is dominated by the cost of computing $\dot{\mathbf{H}}_j^{\exp}$. As explained in Section II-F, the cost of computing $\dot{\mathbf{H}}_j^{\exp}$ (by the explicit MOT schemes) is same as that of $\dot{\mathbf{H}}_j^{\mathrm{imp}}$ (by the implicit MOT schemes). Therefore, C is assumed same for all schemes. Note that this computation could be accelerated using the time-domain adaptive integral method [40], [50]–[54] or (multilevel) plane wave time-domain algorithm [24], [25], [28], [39], [55], [56].

The differences between the explicit schemes and their implicit counterparts are the other operations executed at a given time step. The computational costs of these operations are represented by $C_{\mathrm{PT}}^{\exp}$, $C_{\mathrm{GT}}^{\exp}$, and C^{imp} for explicit schemes with point and Galerkin testing and the implicit scheme, respectively. The estimates for $C_{\mathrm{PT}}^{\exp}$ and $C_{\mathrm{GT}}^{\exp}$ are obtained by following (17)–(22) step by step.

The k-step predictor update in (17) and the k-step corrector update in (20) require $O(2k[2N])$ and $O(m_{\max}[2k+1][2N])$ operations, respectively. Updating the right-hand sides of (18) and (21) requires the computation of $\mathbf{M}_0^{\exp}\mathbf{H}_j$ once and $\mathbf{M}_0^{\exp}\mathbf{H}_j^{(m)}$ $m_{\max}$ times. Assuming γ represents the sparseness factor of $\mathbf{M}_0^1$ and $\mathbf{M}_0^2$, these updates require $O([m_{\max} + 1]2[\gamma N])$ operations in total for predictor and corrector steps. Solution of (19) and (22) has two different complexities depending on the testing procedure used. For point testing, computing the solution requires multiplying the right-hand side with pre-computed sparse $\mathbf{G}^{-1}$ (see Section II-E), resulting in $O([m_{\max} + 1][4N])$ operations in total for predictor and corrector steps. For Galerkin testing $\mathbf{G}$ is sparse without a specific structure (see Section II-E) and the solution is obtained using an iterative solver. This results in $O([m_{\max}+1] N_{\mathrm{iter}}^{\mathrm{G}} F_{\mathrm{iter}} 2[\delta N])$ operations in total for predictor and corrector steps. Here $N_{\mathrm{iter}}^{\mathrm{G}}$ is the number of iterations, F_{iter} is the number of matrix–vector multiplications required at each iteration, and δ is the sparseness factor of $\mathbf{G}$.

The implicit MOT scheme always uses an iterative method to solve (24), which results in $C^{\mathrm{imp}} \sim O(N_{\mathrm{iter}}^{\mathrm{imp}} F_{\mathrm{iter}} 2[(\gamma + \delta)N])$. Here $N_{\mathrm{iter}}^{\mathrm{imp}}$ is the number of iterations and F_{iter} is the number of matrix–vector multiplications required at a given iteration (it is assumed that the explicit and implicit schemes use the same iterative solver).

In the complexity estimates above, k depends on the order/type of the PE(CE)^m; therefore, it is considered as a user-defined input. Also, $N_{\mathrm{iter}}^{\mathrm{G}}$ is always small since $\mathbf{G}$ is well conditioned and sparse regardless of Δt. Assuming $m_{\max}$ is the same for explicit schemes with point and Galerkin testing, the former scheme is faster since $4 \ll N_{\mathrm{iter}}^{\mathrm{G}} F_{\mathrm{iter}} 2\delta$. Numerical results in Section III show that the value of

$m_{\max}$ averaged over all time steps is similar for both the schemes.

Under high-frequency excitations when $c_0 \Delta t$ is comparable to the spatial discretization length, $\gamma \ll N$ and a direct comparison of $C_{\mathrm{PT}}^{\exp}$ and $C_{\mathrm{GT}}^{\exp}$ to C^{imp} becomes challenging since it is difficult to accurately estimate which contributions discussed above are dominant.

Under low-frequency excitations when $c_0 \Delta t$ is comparable to or larger than the size of the scatterer, $\gamma \sim N$, which means that $\mathbf{M}_0^1$ and $\mathbf{M}_0^2$ become fuller. Consequently, $C^{\mathrm{imp}} \sim O(N_{\mathrm{iter}}^{\mathrm{imp}} F_{\mathrm{iter}} N^2)$ (assuming $\gamma \sim N \gg \delta$), $C_{\mathrm{PT}}^{\exp} \sim O(m_{\max} N^2)$ (assuming $\gamma \sim N \gg k$) and $C_{\mathrm{GT}}^{\exp} \sim O(m_{\max} N^2)$ (assuming $\gamma \sim N \gg k$ and $\gamma \sim N \gg N_{\mathrm{iter}}^{\mathrm{G}} F_{\mathrm{iter}} 2\delta$). This means that the explicit schemes are faster than their implicit counterparts as long as $m_{\max} < N_{\mathrm{iter}}^{\mathrm{imp}} F_{\mathrm{iter}}$. Numerical results presented in Section III show that this condition is indeed satisfied.

Note that one can use the low-frequency extension of the time-domain adaptive integral method [57] to accelerate the matrix–vector multiplication $\mathbf{M}_0^{\mathrm{imp}}\mathbf{H}_j$ required by the iterative method to solve (23). However, the same extension can also be used to accelerate the computation of the matrix–vector multiplication $\mathbf{M}_0^{\exp}\mathbf{H}_j$ required by the explicit scheme during the predictor updates. Therefore, the conclusions drawn above are still applicable even when acceleration methods are used.

III. NUMERICAL RESULTS

This section presents numerical examples to demonstrate the advantages of the proposed explicit MOT schemes. In all examples, the scatterer is illuminated by a plane wave traveling in the $\hat{\mathbf{z}}$ direction with a $\hat{\mathbf{y}}$-directed magnetic field

$$\mathbf{H}^{\mathrm{inc}}(\mathbf{r}, t) = \hat{\mathbf{y}} H_0 G(t - \mathbf{r} \cdot \hat{\mathbf{z}}/c_0) \tag{27}$$

where $H_0 = \sqrt{\epsilon_0/\mu_0}$ A/m is the amplitude and $G(t) = \cos[2\pi f_0(t - t_p)]e^{-(t-t_p)^2/(2\sigma^2)}$ is the modulated Gaussian pulse. Here $\sigma = 3/(2\pi f_{\mathrm{bw}})$ is the duration, f_{bw} is the effective bandwidth, f_0 is the center frequency, and $f_{\max} = f_0 + f_{\mathrm{bw}}$ is the maximum frequency of the pulse. It is assumed that the scatterer resides in free space. In all examples, the order of the piecewise polynomial Lagrange interpolation function $T(t)$ $t_{\max} = 4$ [40], and the volume integrals present in the entries of the matrices in (8) and (13), and the vector in (9) are computed using the third-order Gauss-Legendre quadrature rule [45], [46].

The accuracy, efficiency, and stability of the four MOT schemes are compared. The implicit scheme with point testing, the explicit scheme with point testing, the implicit scheme with Galerkin testing, and the explicit scheme with Galerkin testing. For the sake of briefness, in the rest of this section, these schemes are referred to using the notations $[\mathrm{MOT}]_{\mathrm{PT}}^{\mathrm{imp}}$, $[\mathrm{MOT}]_{\mathrm{PT}}^{\exp}$, $[\mathrm{MOT}]_{\mathrm{GT}}^{\mathrm{imp}}$, and $[\mathrm{MOT}]_{\mathrm{GT}}^{\exp}$, respectively.

$[\mathrm{MOT}]_{\mathrm{PT}}^{\mathrm{imp}}$, $[\mathrm{MOT}]_{\mathrm{GT}}^{\mathrm{imp}}$, and $[\mathrm{MOT}]_{\mathrm{GT}}^{\exp}$ use the transpose-free quasi-minimal residual (TFQMR) method [58] to iteratively solve the relevant matrix equations. All TFQMR iterations are diagonally preconditioned. $[\mathrm{MOT}]_{\mathrm{PT}}^{\mathrm{imp}}$ and $[\mathrm{MOT}]_{\mathrm{GT}}^{\mathrm{imp}}$ start the TFQMR iterations at time step l with initial guess $\mathbf{H}_l = 2\mathbf{H}_{l-1} - \mathbf{H}_{l-2}$. The TFQMR iterations and the correction

updates of the $[\text{MOT}]_{\text{PT}}^{\text{exp}}$ and $[\text{MOT}]_{\text{GT}}^{\text{exp}}$ are terminated when the following stopping criterion is satisfied:

$$\left\| \mathbf{I}_l^u - \mathbf{I}_l^{u-1} \right\| < \chi \left\| \mathbf{I}_{l-1} \right\|. \tag{28}$$

Here $\mathbf{I}_l^u$ represents the solution vector at the lth time step and the uth TFQMR iteration or at the lth time step and the uth correction update, and χ is the convergence threshold. $\chi = 10^{-6}$ unless specified otherwise. The PE(CE)^m scheme uses the fourth-order Adam-Bashworth and backward difference coefficients at the prediction and correction steps, respectively [41].

After the time-domain simulations are completed, the solutions are Fourier transformed and divided by the Fourier transform of $G(t)$ to yield the time harmonic magnetic field, $\tilde{\mathbf{H}}(\mathbf{r}, f)$. Time harmonic electric field $\tilde{\mathbf{E}}(\mathbf{r}, f)$ and the time harmonic current density $\tilde{\mathbf{J}}(\mathbf{r}, f)$ are computed by taking the curl of (4). The radar cross section (RCS) is computed using $\tilde{\mathbf{J}}(\mathbf{r}, f)$. Let $\sigma_{\text{PT}}^{\text{imp}}(\theta, \phi, f)$, $\sigma_{\text{PT}}^{\text{exp}}(\theta, \phi, f)$, $\sigma_{\text{GT}}^{\text{imp}}(\theta, \phi, f)$, and $\sigma_{\text{GT}}^{\text{exp}}(\theta, \phi, f)$ represent the RCS obtained from $\tilde{\mathbf{J}}(\mathbf{r}, f)$ computed by the $[\text{MOT}]_{\text{PT}}^{\text{imp}}$, $[\text{MOT}]_{\text{PT}}^{\text{exp}}$, $[\text{MOT}]_{\text{GT}}^{\text{imp}}$, and $[\text{MOT}]_{\text{GT}}^{\text{exp}}$, respectively, along the direction defined by θ and ϕ. To compare the accuracy of $[\text{MOT}]_{\text{PT}}^{\text{imp}}$, $[\text{MOT}]_{\text{PT}}^{\text{exp}}$, $[\text{MOT}]_{\text{GT}}^{\text{imp}}$, and $[\text{MOT}]_{\text{GT}}^{\text{exp}}$, L_2-norm error in RCS, which is defined as

$$err^{\text{RCS}} = \sqrt{\frac{\sum_{n=0}^{360} \left| \sigma^{\text{ref}}(n\Delta\theta, \phi, f) - \sigma_{\text{test}}^{\text{type}}(n\Delta\theta, \phi, f) \right|^2}{\sum_{n=0}^{360} \left| \sigma^{\text{ref}}(n\Delta\theta, \phi, f) \right|^2}} \tag{29}$$

is used. Here type $\in \{\text{imp}, \text{exp}\}$, test $\in \{\text{GT}, \text{PT}\}$, ref $\in \{\text{Mie}, \text{FD}\}$, $\Delta\theta = 0.5°$, and $\phi = 0°$. In (29), $\sigma^{\text{Mie}}(\theta, \phi, f)$ and $\sigma^{\text{FD}}(\theta, \phi, f)$ refer to the RCS obtained from the Mie series solution or $\tilde{\mathbf{J}}(\mathbf{r}, f)$ computed by an FD-EFVIE solver. The FD-EFVIE solver uses the same mesh as the MOT schemes but discretizes the electric flux density using SWG basis and testing functions [33]. The entries of the resulting method of moments (MoM) matrix are computed using the third-order Gauss-Legendre quadrature rule [45], [46]. The MoM system is solved using the TFQMR method. The iterations are truncated when $\|\tilde{\mathbf{Z}}\tilde{\mathbf{I}}^u - \tilde{\mathbf{Z}}\tilde{\mathbf{I}}^{u-1}\| < 10^{-6}\|\tilde{\mathbf{V}}^{\text{inc}}\|$, where $\tilde{\mathbf{I}}^u$, $\tilde{\mathbf{Z}}$, and $\tilde{\mathbf{V}}^{\text{inc}}$ represent the solution at the uth iteration, the MoM matrix, and the right-hand side vector, respectively.

A. Accuracy of the FLC and Nedelec Basis Functions

In this example, the scatterer is a sphere with radius 2 m and permittivity ε_0. Since $\kappa(\mathbf{r}) = 0$, $\mathbf{H}^{\text{sca}}(\mathbf{r}, t) = 0$ and $\mathbf{H}(\mathbf{r}, t) = \mathbf{H}^{\text{inc}}(\mathbf{r}, t)$, i.e. the solution should match the incident field. The excitation parameters $f_0 = 10$ MHz and $f_{\text{bw}} = 5$ MHz. Six different meshes are used. The average edge length of these meshes, l_{av}, changes from 134.37 cm ($\lambda_0/22.32$) to 38.58 cm ($\lambda_0/77.75$). Here, $\lambda_0 = c_0/f_0$ is the free-space wavelength at f_0. Three different Δt are considered: 6.667 ns ($0.1/f_{\text{max}}$), 10 ns ($0.15/f_{\text{max}}$), and 13.333 ns ($0.2/f_{\text{max}}$). Two sets of simulations are carried out using the $[\text{MOT}]_{\text{GT}}^{\text{exp}}$ for every combination of l_{av} and Δt. In the first set, $\mathbf{H}(\mathbf{r}, t)$ is expanded using the Nedelec functions [only $\mathbf{f}_n^2(\mathbf{r})$ in (4)]; while in the second set, FLC basis functions are used [both $\mathbf{f}_n^1(\mathbf{r})$ and $\mathbf{f}_n^2(\mathbf{r})$ in (4)]. To compare the accuracy of the simulations,

L_2-norm errors in $\tilde{\mathbf{E}}(\mathbf{r}, f)$ and $\tilde{\mathbf{H}}(\mathbf{r}, f)$, which are defined as

$$err^{\text{E}} = \sqrt{\frac{\sum_{k=1}^{N_v} \left| \tilde{\mathbf{E}}(\mathbf{r}_k, f) - \tilde{\mathbf{E}}^{\text{inc}}(\mathbf{r}_k, f) \right|^2}{\sum_{k=1}^{N_v} \left| \tilde{\mathbf{E}}^{\text{inc}}(\mathbf{r}_k, f) \right|^2}} \tag{30}$$

$$err^{\text{H}} = \sqrt{\frac{\sum_{k=1}^{N_v} \left| \tilde{\mathbf{H}}(\mathbf{r}_k, f) - \tilde{\mathbf{H}}^{\text{inc}}(\mathbf{r}_k, f) \right|^2}{\sum_{k=1}^{N_v} \left| \tilde{\mathbf{H}}^{\text{inc}}(\mathbf{r}_k, f) \right|^2}} \tag{31}$$

are used. Here $\mathbf{r}_k$ represent the centers of the tetrahedrons and N_v is their number, $\{\tilde{\mathbf{E}}^{\text{inc}}(\mathbf{r}, f), \tilde{\mathbf{H}}^{\text{inc}}(\mathbf{r}, f)\}$ are the time harmonic incident electric and magnetic fields, and $f = f_0$. Fig. 1(a) and (b) plot err^{H} and err^{E} versus λ_0/l_{av}, respectively, for the simulations with only $\mathbf{f}_n^2(\mathbf{r})$ executed for three different Δt. Fig. 1(a) and (b) show that err^{H} decreases with increasing mesh density and decreasing Δt, while err^{E} remains high even for the densest mesh and the smallest Δt. Fig. 1(c) and (d) do the same comparison for simulations with $\mathbf{f}_n^1(\mathbf{r}) \cup \mathbf{f}_n^2(\mathbf{r})$. Both err^{H} and err^{E} decrease with increasing mesh density and decreasing Δt. Fig. 1(c) and (d) clearly show that using only $\mathbf{f}_n^2(\mathbf{r})$ results in an inaccurate representation of $\mathbf{E}(\mathbf{r}, t)$, while using $\mathbf{f}_n^1(\mathbf{r}) \cup \mathbf{f}_n^2(\mathbf{r})$ renders $\mathbf{E}(\mathbf{r}, t)$ as accurate as $\mathbf{H}(\mathbf{r}, t)$. In other words, $\mathbf{f}_n^2(\mathbf{r})$ accurately represent the solution, but the curl of the resulting solution is not accurate. When $\kappa(\mathbf{r}) \neq 0$, the curl of the solution is needed to compute $\dot{\mathbf{H}}_j^{\text{sca},p}$, $p \in \{1, 2\}$ [see (10)]. This means that using only $\mathbf{f}_n^2(\mathbf{r})$ makes the MOT solution inaccurate (and consequently unstable). The results and the discussion presented in this section clearly justify why $\mathbf{f}_n^1(\mathbf{r}) \cup \mathbf{f}_n^2(\mathbf{r})$ are used by the MOT schemes developed in this article.

Fig. 1(c) and (d) also show that err^{H} and err^{E} decrease with a rate roughly between $(l_{\text{av}})^{-1}$ (for large Δt) and $(l_{\text{av}})^{-2}$ (for small Δt) for $\lambda_0/32 > l_{\text{av}} > \lambda_0/45$ and with a rate around $(l_{\text{av}})^{-1}$ for $l_{\text{av}} < \lambda_0/45$. This decrease in the convergence rate can be explained by the fact that for small l_{av}, the dominant error comes from the temporal discretization. This is demonstrated in Fig. 1(c) and (d); for smaller Δt, the "flattening" of err^{H} and err^{E} curves starts at smaller l_{av}. In other words, for small l_{av}, the accuracy can further be increased by reducing Δt.

B. Late Time Stability

For this example, scattering from a sphere with radius 1 m and permittivity $10\varepsilon_0$ is analyzed for different values of the convergence threshold χ. The sphere is discretized using 5350 tetrahedrons resulting in $N = 13\,494$ unknowns. The excitation parameters $f_0 = 10$ MHz and $f_{\text{bw}} = 5$ MHz. The average, minimum, and maximum edge length of the mesh are $l_{\text{av}} = \lambda_{\text{min}}/33.28$, $l_{\text{min}} = \lambda_{\text{min}}/62.0$, and $l_{\text{max}} = \lambda_{\text{min}}/19.76$, respectively. Here $\lambda_{\text{min}} = c_0/(\sqrt{10}f_{\text{max}})$ is the wavelength at f_{max} inside the scatterer. All four MOT schemes are executed for $N_t = 1200$ with $\Delta t = 6.667$ ns ($0.1/f_{\text{max}}$) and three different $\chi \in \{10^{-6}, 10^{-8}, 10^{-10}\}$. Fig. 2(a)–(c) plot $\mathbf{H}(\mathbf{r}, t)$ computed by these schemes at point $\mathbf{r} = (0.51, -0.64, 0.12)$ m for $\chi = 10^{-6}$, $\chi = 10^{-8}$, and $\chi = 10^{-10}$, respectively, and show that all four schemes provide stable results with a very small dc component and that the amplitude of the dc component can be further reduced by decreasing χ.
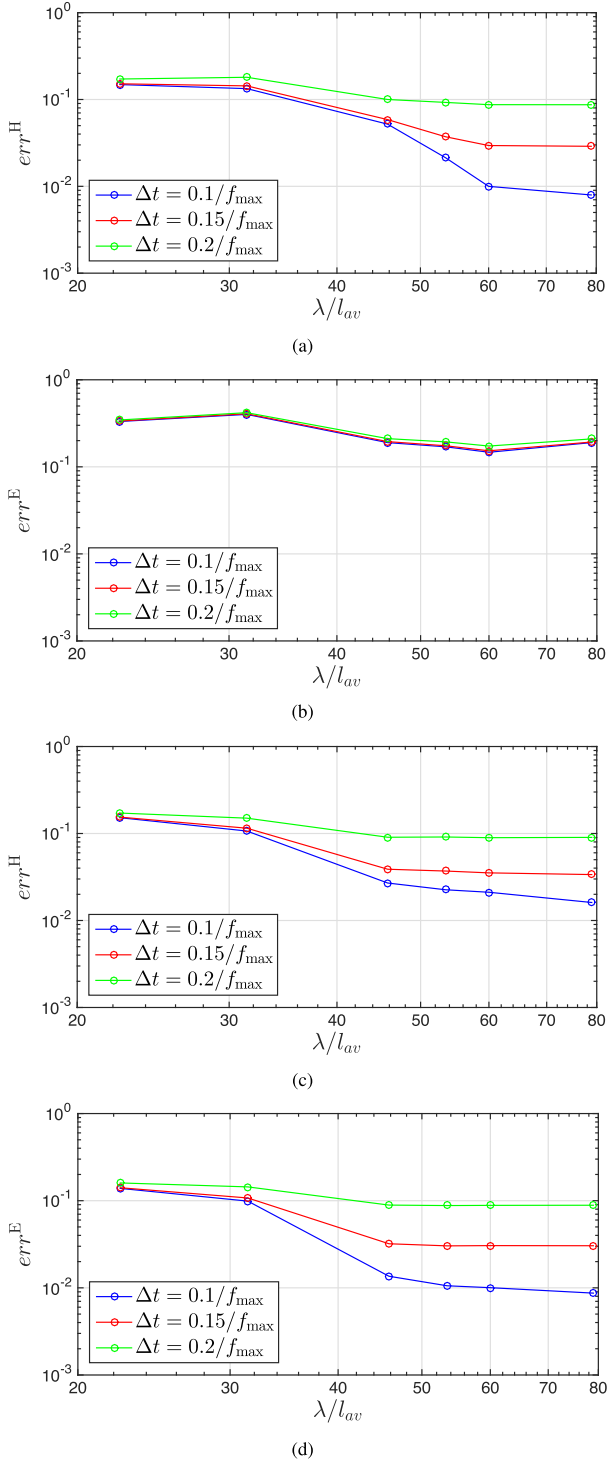
Fig. 1. Comparison of the accuracy of the Nedelec basis functions $\mathbf{f}_n^2(\mathbf{r})$ and the FLC basis functions $\mathbf{f}_n^1(\mathbf{r}) \cup \mathbf{f}_n^2(\mathbf{r})$. (a) err^H and (b) err^E versus λ_0/l_{av} for simulations using $\mathbf{f}_n^2(\mathbf{r})$ with three different Δt. (c) err^H and (d) err^E versus λ_0/l_{av} for simulations using $\mathbf{f}_n^1(\mathbf{r}) \cup \mathbf{f}_n^2(\mathbf{r})$ with three different Δt.

Fig. 2. Analysis of scattering from a sphere with radius 1 m and permittivity $10\varepsilon_0$. $\mathbf{H}(\mathbf{r}, t)$ computed at point $\mathbf{r} = (0.51, -0.64, 0.12)$ m by all four MOT schemes with (a) $\chi = 10^{-6}$, (b) $\chi = 10^{-8}$, and (c) $\chi = 10^{-10}$.

C. Unit Sphere

In this section, the efficiency and accuracy of $[\text{MOT}]_{\text{PT}}^{\text{imp}}$, $[\text{MOT}]_{\text{PT}}^{\text{exp}}$, $[\text{MOT}]_{\text{GT}}^{\text{imp}}$, and $[\text{MOT}]_{\text{GT}}^{\text{exp}}$ are compared. To this end, scattering from a sphere with radius 1 m is analyzed. First, the permittivity of the sphere is set to $10\varepsilon_0$. The sphere
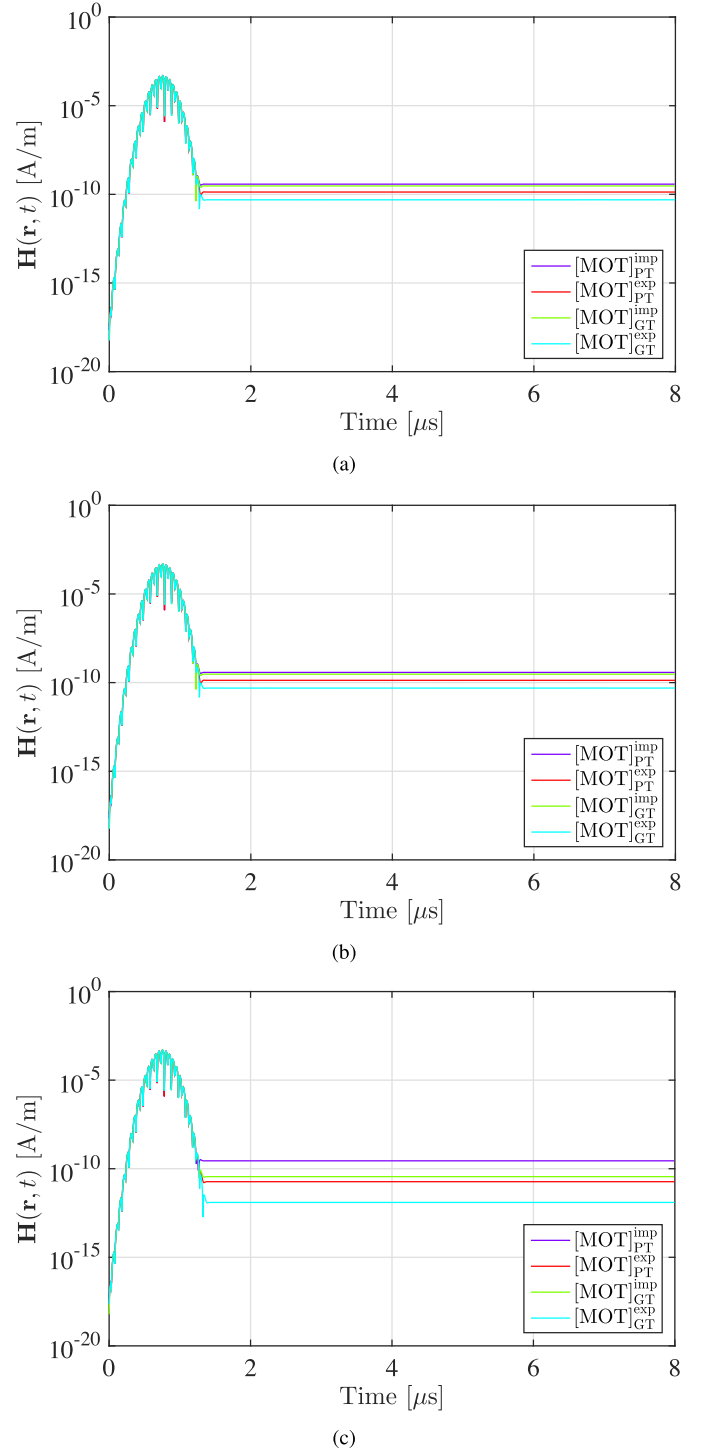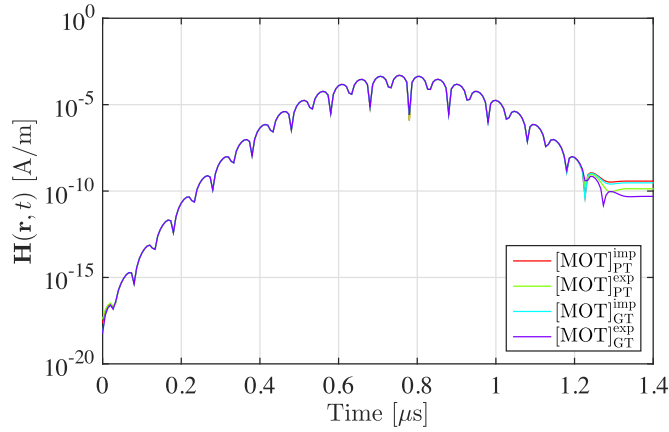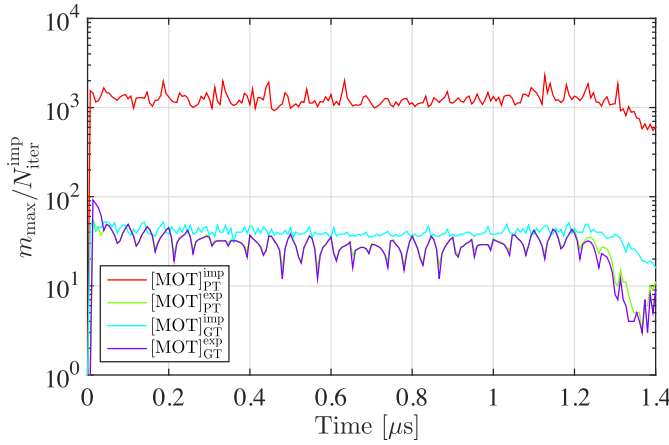
is discretized using 5350 tetrahedrons resulting in $N = 13\,494$ unknowns. The excitation parameters $f_0 = 10$ MHz and $f_{\text{bw}} = 5$ MHz. The average, minimum, and maximum edge length of the mesh are $l_{\text{av}} = \lambda_{\text{min}}/33.28$, $l_{\text{min}} = \lambda_{\text{min}}/62.0$, and $l_{\text{max}} = \lambda_{\text{min}}/19.76$, respectively. Here $\lambda_{\text{min}} = c_0/(\sqrt{10}f_{\text{max}})$ is the wavelength at f_{max} inside the scatterer. All four schemes are executed three times for $N_t = 210$ with

(a)

(b)
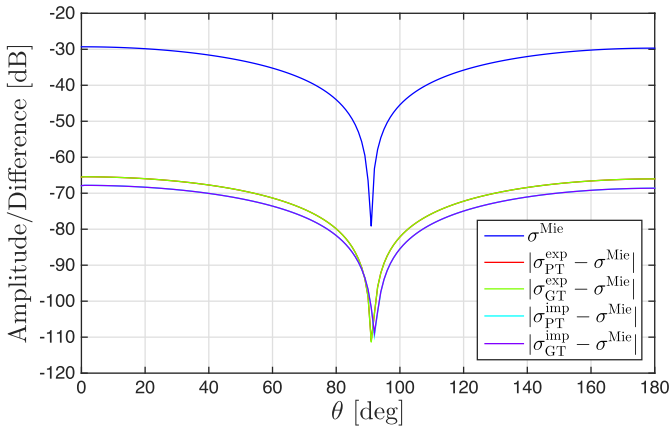
(c)

Fig. 3.   Analysis of scattering from a sphere with radius 1 m and permittivity $10\varepsilon_0$. (a) $\mathbf{H}(\mathbf{r}, t)$ computed at point $\mathbf{r} = (0.51, -0.64, 0.12)$ m by all four MOT schemes. (b) $m_{\max}/N_{\text{iter}}^{\text{imp}}$ required by the explicit/implicit MOT schemes. (c) Comparison of RCS computed for $0° < \theta < 180°$ and $\phi = 0°$ at $f = 10$ MHz by the MOT schemes to that computed from the Mie series solution.

$\Delta t = 6.667$ ns $(0.1/f_{\max})$, $N_{\text{t}} = 140$ with $\Delta t = 10$ ns $(0.15/f_{\max})$, and $N_{\text{t}} = 105$ with $\Delta t = 13.333$ ns $(0.2/f_{\max})$. For all simulations, the sparseness factor of $\mathbf{M}_0^1$ and $\mathbf{M}_0^2$ is $\gamma = N$ and the sparseness factor of $\mathbf{G}$ is $\delta = 0.0031N$.
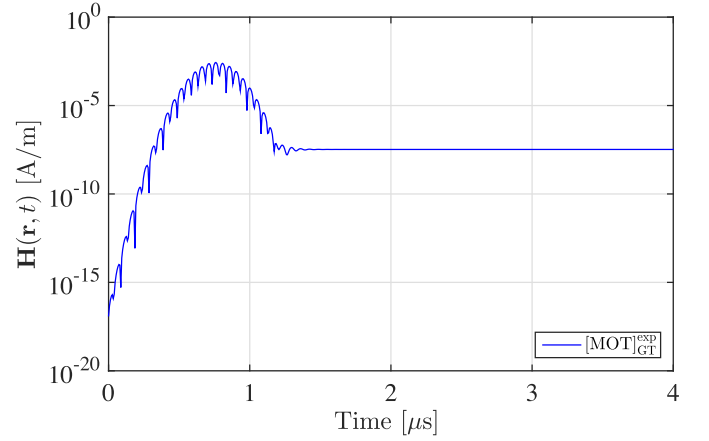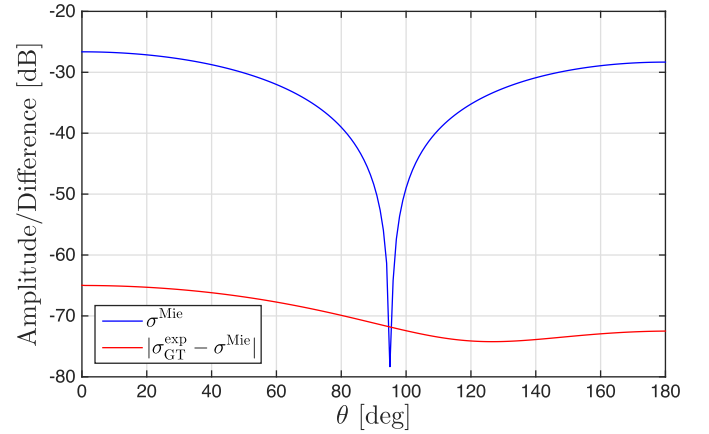

(a)

(b)

Fig. 4.   Analysis of scattering from a sphere with radius 1 m and permittivity $50\varepsilon_0$. (a) $\mathbf{H}(\mathbf{r}, t)$ computed at point $\mathbf{r} = (0.51, -0.64, 0.12)$ m by $[\text{MOT}]_{\text{GT}}^{\text{exp}}$. (b) Comparison of RCS computed for $0° < \theta < 180°$ and $\phi = 0°$ at $f = 10$ MHz by $[\text{MOT}]_{\text{GT}}^{\text{exp}}$ to that computed from the Mie series solution.

Fig. 3(a) plots $\mathbf{H}(\mathbf{r}, t)$ computed by all four schemes at point $\mathbf{r} = (0.51, -0.64, 0.12)$ m for the set of simulations with $\Delta t = 6.667$ ns. Fig. 3(a) shows that all four schemes provide practically the same result. For the same set of simulations, Fig. 3(b) plots the number of correction updates $m_{\max}$ required by the $[\text{MOT}]_{\text{PT}}^{\text{exp}}$ and $[\text{MOT}]_{\text{GT}}^{\text{exp}}$ as well as the number of TFQMR iterations $N_{\text{iter}}^{\text{imp}}$ required by the $[\text{MOT}]_{\text{PT}}^{\text{imp}}$ and $[\text{MOT}]_{\text{GT}}^{\text{imp}}$ to achieve the convergence criterion in (28) at every time step. For $[\text{MOT}]_{\text{PT}}^{\text{imp}}$ and $[\text{MOT}]_{\text{GT}}^{\text{imp}}$, $N_{\text{iter}}^{\text{imp}}$ reaches roughly 1500 and 50, respectively. For $[\text{MOT}]_{\text{PT}}^{\text{exp}}$ and $[\text{MOT}]_{\text{GT}}^{\text{exp}}$, $m_{\max}$ reaches roughly 40. The number of iterations required to solve (19) and (22) is $N_{\text{iter}}^{\text{G}} = 22$. Inserting these values in the computational complexity estimates described in Section II-G shows that $[\text{MOT}]_{\text{PT}}^{\text{exp}}$ is faster than $[\text{MOT}]_{\text{GT}}^{\text{exp}}$, which is faster than both $[\text{MOT}]_{\text{GT}}^{\text{imp}}$ and $[\text{MOT}]_{\text{PT}}^{\text{imp}}$. Indeed, measured computation times, which are presented in Table I's first group of rows, verify this result. Note that in Table I, the fourth column T_{fill} is the time required to compute all relevant matrices, the fifth column T_{MOT} refers to $C_{\text{PT}}^{\text{exp}} N_{\text{t}} + C$, $C_{\text{GT}}^{\text{exp}} N_{\text{t}} + C$, or $C^{\text{imp}} N_{\text{t}} + C$ (see Section II-G) depending on

the scheme used, and the sixth column T_{tot} is the sum of the previous two.

For the same set of simulations with $\Delta t = 6.667$ ns, Fig. 3(c) compares $\sigma_{\text{PT}}^{\text{imp}}(\theta, \phi, f)$, $\sigma_{\text{PT}}^{\text{exp}}(\theta, \phi, f)$, $\sigma_{\text{GT}}^{\text{imp}}(\theta, \phi, f)$, and $\sigma_{\text{GT}}^{\text{exp}}(\theta, \phi, f)$ to $\sigma^{\text{Mie}}(\theta, \phi, f)$, all of which are computed for $0° < \theta < 180°$ and $\phi = 0°$ at $f = f_0$, and shows that all four MOT schemes practically have the same accuracy. Additionally, the last column of the first group of rows in Table I provides err^{RCS} computed using (29) for this set of simulations and confirms that all four MOT schemes have the same level of accuracy.

Table I's second and third groups of rows compares the efficiency and accuracy of the MOT schemes for the sets of simulations with $\Delta t = 10$ ns and $\Delta t = 13.333$ ns. Same conclusions can be drawn: All four MOT schemes have the same level of accuracy, and $[\text{MOT}]_{\text{PT}}^{\text{exp}}$ is significantly faster than the other three. Table I also shows that the accuracy of all schemes increases with decreasing Δt.

Next, the permittivity of the sphere is set to $50\varepsilon_0$. The sphere is discretized using 11697 tetrahedrons, resulting in $N = 28970$ unknowns. The average, minimum, and maximum edge length of the mesh are $l_{\text{av}} = \lambda_{\min}/19.51$, $l_{\min} = \lambda_{\min}/39.34$, and $l_{\max} = \lambda_{\min}/11.55$, respectively. Here $\lambda_{\min} = c_0/(\sqrt{50}f_{\max})$ is the wavelength at $f_{\max}$ inside the scatterer. $[\text{MOT}]_{\text{GT}}^{\text{exp}}$ is executed three times for $N_t = 600$ with $\Delta t = 6.667$ ns ($0.1/f_{\max}$), $N_t = 400$ with $\Delta t = 10$ ns ($0.15/f_{\max}$), and $N_t = 300$ with $\Delta t = 13.333$ ns ($0.2/f_{\max}$).

Fig. 4(a) plots $\mathbf{H}(\mathbf{r}, t)$ computed at point $\mathbf{r} = (0.51, -0.64, 0.12)$ m for the simulation with $\Delta t = 6.667$ ns. Note that for this problem, the other three schemes do not produce stable results. For the same simulation, Fig. 4(b) compares $\sigma_{\text{GT}}^{\text{exp}}(\theta, \phi, f)$ to $\sigma^{\text{Mie}}(\theta, \phi, f)$, both of which are computed for $0° < \theta < 180°$ and $\phi = 0°$ at $f = f_0$. Results agree very well. Table II provides the computation times and accuracy of $[\text{MOT}]_{\text{GT}}^{\text{exp}}$ for all three simulations. It shows that the accuracy increases with decreasing Δt.

D. Piecewise Slab

In the last example, scattering from a piecewise dielectric slab is analyzed. The slab consists of two equal volumes with permittivities $3\varepsilon_0$ and $9\varepsilon_0$ [as shown in the inset of Fig. 5(a)]. The slab is discretized using 7905 tetrahedrons resulting in $N = 20\,570$ unknowns. The excitation parameters $f_0 = 10$ MHz and $f_{\text{bw}} = 5$ MHz. The average, minimum, and maximum edge length of the mesh are $l_{\text{av}} = \lambda_{\min}/31.7$, $l_{\min} = \lambda_{\min}/66.6$, and $l_{\max} = \lambda_{\min}/19$, respectively. Here $\lambda_{\min} = c_0/(\sqrt{9}f_{\max})$ is the wavelength at $f_{\max}$ inside the right side of the slab. All four schemes are executed three times for $N_t = 210$ with $\Delta t = 6.667$ ns ($0.1/f_{\max}$), $N_t = 140$ with $\Delta t = 10$ ns ($0.15/f_{\max}$), and $N_t = 105$ with $\Delta t = 13.333$ ns ($0.2/f_{\max}$). For all simulations, the sparseness factor of $\mathbf{M}_0^1$ and $\mathbf{M}_0^2$ is $\gamma = N$ and the sparseness factor of $\mathbf{G}$ is $\delta = 0.0033N$.

Fig. 5(a) plots $\mathbf{H}(\mathbf{r}, t)$ computed by all four schemes at point $\mathbf{r} = (0.23, 0.14, 0.57)$ m for the set of simulations with $\Delta t = 6.667$ ns. The results agree very well. For the same set of simulations, Fig. 5(b) plots the number of correction
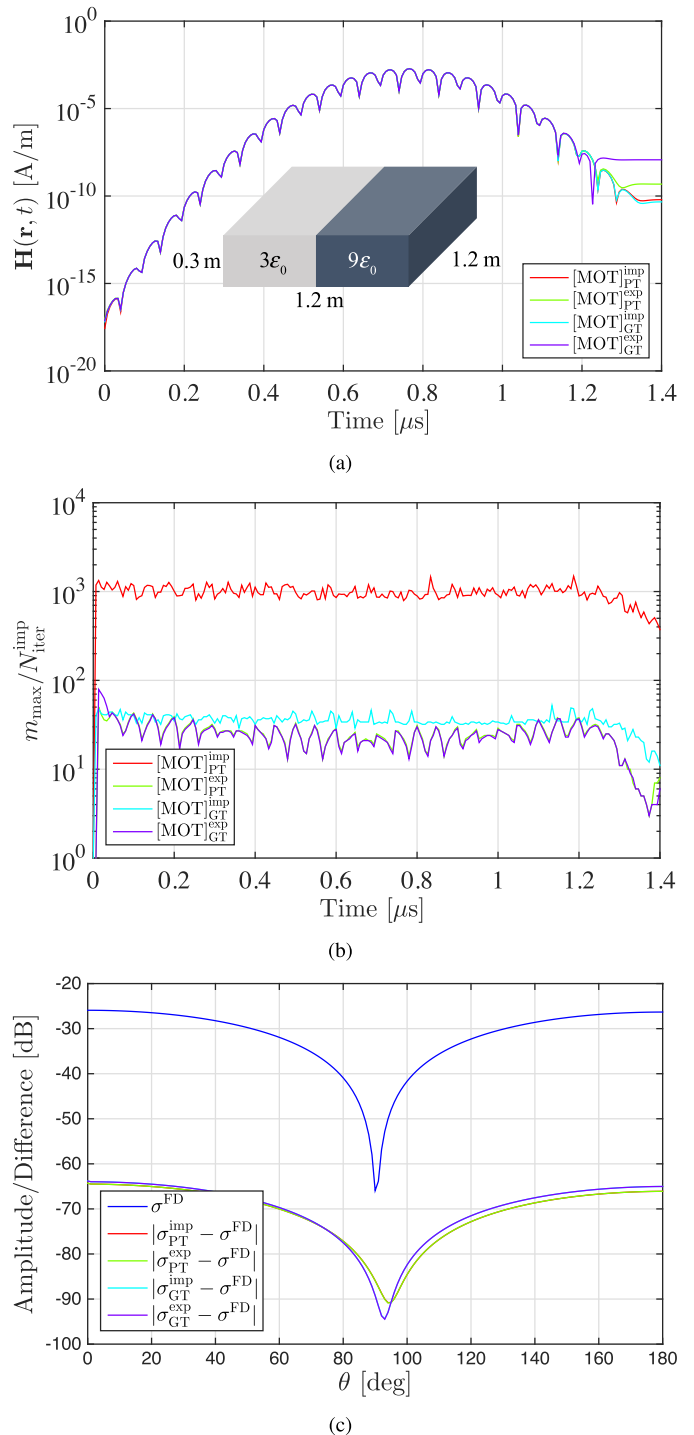
Fig. 5. Analysis of scattering from the piecewise slab shown in the inset of (a) $\mathbf{H}(\mathbf{r}, t)$ computed at point $\mathbf{r} = (0.23, 0.14, 0.57)$ m by all four MOT schemes. (b) $m_{\max}/N_{\text{iter}}^{\text{imp}}$ required by the explicit/implicit MOT schemes. (c) Comparison of RCS computed for $0° < \theta < 180°$ and $\phi = 0°$ at $f = 10$ MHz by the MOT schemes to that obtained from solution computed by the FD-EFVIE solver.

updates $m_{\max}$ required by the $[\text{MOT}]_{\text{PT}}^{\text{exp}}$ and $[\text{MOT}]_{\text{GT}}^{\text{exp}}$ as well as the number of TFQMR iterations $N_{\text{iter}}^{\text{imp}}$ required by the $[\text{MOT}]_{\text{PT}}^{\text{imp}}$ and $[\text{MOT}]_{\text{GT}}^{\text{imp}}$ to achieve the convergence criterion in (28) at every time step. The number of iterations required to solve (19) and (22) ($N_{\text{iter}}^{\text{G}}$) is 21. Inserting these values

TABLE I

EFFICIENCY AND ACCURACY OF THE FOUR MOT SCHEMES IN ANALYZING SCATTERING FROM THE UNIT SPHERE WITH PERMITTIVITY $10\varepsilon_0$

Δt (ns)	N_t	MOT	T_{fill} (s)	T_{MOT} (s)	T_{tot} (s)	$\Sigma N_{\text{iter}}^{\text{imp}}$ / Σm_{max}	err^{RCS}
6.667	210	$[\text{MOT}]_{\text{PT}}^{\text{imp}}$	55	12847	12902	258121	0.0152
		$[\text{MOT}]_{\text{PT}}^{\text{exp}}$	57	297	354	6152	0.0152
		$[\text{MOT}]_{\text{GT}}^{\text{imp}}$	965	499	1464	8277	0.0114
		$[\text{MOT}]_{\text{GT}}^{\text{exp}}$	966	253	1219	6089	0.0114
10	140	$[\text{MOT}]_{\text{PT}}^{\text{imp}}$	55	9274	9328	185833	0.0357
		$[\text{MOT}]_{\text{PT}}^{\text{exp}}$	57	206	263	6476	0.0357
		$[\text{MOT}]_{\text{GT}}^{\text{imp}}$	963	295	1258	6888	0.0364
		$[\text{MOT}]_{\text{GT}}^{\text{exp}}$	964	248	1211	6383	0.0364
13.333	105	$[\text{MOT}]_{\text{PT}}^{\text{imp}}$	55	6636	6691	145932	0.109
		$[\text{MOT}]_{\text{PT}}^{\text{exp}}$	57	200	257	6637	0.109
		$[\text{MOT}]_{\text{GT}}^{\text{imp}}$	962	256	1218	4926	0.110
		$[\text{MOT}]_{\text{GT}}^{\text{exp}}$	963	238	1201	4517	0.110

TABLE II

EFFICIENCY AND ACCURACY OF $[\text{MOT}]_{\text{GT}}^{\text{exp}}$ IN ANALYZING SCATTERING FROM THE UNIT SPHERE WITH $\varepsilon_{\mathbf{r}} = 50$

Δt (ns)	N_t	T_{fill} (s)	T_{MOT} (s)	T_{tot} (s)	Σm_{max}	err^{RCS}
6.667	600	3623	7387	11009	42322	0.012
10	400	3623	7120	10743	42378	0.051
13.33	300	3625	6343	9968	38671	0.129

TABLE III

EFFICIENCY AND ACCURACY OF THE FOUR MOT SCHEMES IN ANALYZING SCATTERING FROM THE PIECEWISE SLAB

Δt (ns)	N_t	MOT	T_{fill} (s)	T_{MOT} (s)	T_{tot} (s)	$\Sigma N_{\text{iter}}^{\text{imp}}$ / Σm_{max}	err^{RCS}
6.667	210	$[\text{MOT}]_{\text{PT}}^{\text{imp}}$	108	23003	23111	204307	0.0113
		$[\text{MOT}]_{\text{PT}}^{\text{exp}}$	111	346	457	5179	0.0113
		$[\text{MOT}]_{\text{GT}}^{\text{imp}}$	1730	917	2647	7390	0.0123
		$[\text{MOT}]_{\text{GT}}^{\text{exp}}$	1734	493	2227	5170	0.0123
10	140	$[\text{MOT}]_{\text{PT}}^{\text{imp}}$	107	18380	18487	162433	0.0458
		$[\text{MOT}]_{\text{PT}}^{\text{exp}}$	111	340	451	5292	0.0458
		$[\text{MOT}]_{\text{GT}}^{\text{imp}}$	1730	642	2372	5171	0.0465
		$[\text{MOT}]_{\text{GT}}^{\text{exp}}$	1735	441	2176	5223	0.0465
13.333	105	$[\text{MOT}]_{\text{PT}}^{\text{imp}}$	107	14314	14421	127842	0.117
		$[\text{MOT}]_{\text{PT}}^{\text{exp}}$	111	345	456	5559	0.117
		$[\text{MOT}]_{\text{GT}}^{\text{imp}}$	1728	522	2250	4377	0.118
		$[\text{MOT}]_{\text{GT}}^{\text{exp}}$	1729	431	2160	5128	0.118

and the ones provided in Fig. 5(b) in the computational complexity estimates described in Section II-G shows that the $[\text{MOT}]_{\text{PT}}^{\text{exp}}$ is faster than the $[\text{MOT}]_{\text{GT}}^{\text{exp}}$, which is faster than both the $[\text{MOT}]_{\text{GT}}^{\text{imp}}$ and $[\text{MOT}]_{\text{PT}}^{\text{imp}}$. This result is verified by the computation times provided in Table III's first group of rows.

For the same set of simulations with $\Delta t = 6.667$ ns, Fig. 5(c) compares $\sigma_{\text{PT}}^{\text{imp}}(\theta, \phi, f)$, $\sigma_{\text{PT}}^{\text{exp}}(\theta, \phi, f)$, $\sigma_{\text{GT}}^{\text{exp}}(\theta, \phi, f)$, and $\sigma_{\text{GT}}^{\text{imp}}(\theta, \phi, f)$ to $\sigma^{\text{FD}}(\theta, \phi, f)$, all of which are computed for $0° < \theta < 180°$ and $\phi = 0°$ at $f = f_0$. Results agree very well. Additionally, the last column

of the first group of rows in Table III provides err^{RCS} computed using (29) for this set of simulations and confirms that all four MOT schemes have the same level of accuracy.

Table III's second and third groups of rows compares the efficiency and accuracy of the MOT schemes for the sets of simulations with $\Delta t = 10$ ns and $\Delta t = 13.333$ ns. The results show that all four MOT schemes have the same level of accuracy, and $[\text{MOT}]_{\text{PT}}^{\text{exp}}$ is significantly faster than the other three. Also, as expected, the accuracy of all schemes increases with decreasing Δt.

IV. Conclusion

A method for constructing explicit MOT schemes to solve the TD-MFVIE enforced on dielectric scatterers is developed. The TD-MFVIE is first cast in the form of an ODE and the unknown magnetic field is expanded using the FLC basis functions. The expansion is inserted into the TD-MFVIE and the resulting equation is Galerkin or point tested in space. This yields an ODE matrix system, which is integrated in time using a PE(CE)^m scheme for the (unknown) expansion coefficients. The resulting MOT scheme calls for the solution of a Gram matrix system at the evaluation (E) steps of every time step. This can be done very efficiently since the Gram matrix is always well conditioned and sparse (for Galerkin testing) or consists of only four diagonal blocks (for point testing). Numerical results demonstrate that the explicit MOT scheme with point testing is significantly faster without sacrificing from accuracy for low-frequency problems.

An extension of the proposed MOT scheme to enable the analysis of electromagnetic scattering from nonlinear dielectric objects is underway.

Acknowledgment

References

[1] A. Taflove and S. C. Hagness, *Computational Electrodynamics: The Finite-Difference Time-Domain Method*. Norwood, MA, USA: Artech House, 2005.

[2] D. M. Sullivan, *Electromagnetic Simulation Using the FDTD Method*. New York, NY, USA: Wiley, 2000.

[3] J. P. Berenger, "Perfectly matched layer for the FDTD solution of wave-structure interaction problems," *IEEE Trans. Antennas Propag.*, vol. 44, no. 1, pp. 110–117, Jan. 1996.

[4] K. Sirenko, V. Pazynin, Y. K. Sirenko, and H. Bagci, "An FFT-accelerated FDTD scheme with exact absorbing conditions for characterizing axially symmetric resonant structures," *Prog. Electromagn. Res.*, vol. 111, pp. 331–364, Jan. 2011.

[5] J.-M. Jin, *The Finite Element Method in Electromagnetics*. Hoboken, NJ, USA: Wiley, 2014.

[6] D. Jiao, M. Lu, E. Michielssen, and J.-M. Jin, "A fast time-domain finite element-boundary integral method for electromagnetic analysis," *IEEE Trans. Antennas Propag.*, vol. 49, no. 10, pp. 1453–1461, Oct. 2001.

[7] D. Jiao, J.-M. Jin, E. Michielssen, and D. J. Riley, "Time-domain finite-element simulation of three-dimensional scattering and radiation problems using perfectly matched layers," *IEEE Trans. Antennas Propag.*, vol. 51, no. 2, pp. 296–305, Feb. 2003.

[8] A. E. Yilmaz, Z. Lou, E. Michielssen, and J. M. Jin, "A single-boundary implicit and FFT-accelerated time-domain finite element-boundary integral solver," *IEEE Trans. Antennas Propag.*, vol. 55, no. 5, pp. 1382–1397, May 2007.

[9] J. S. Hesthaven and T. Warburton, *Nodal Discontinuous Galerkin Methods*. New York, NY, USA: Springer, 2008.

[10] M. Liu, K. Sirenko, and H. Bagci, "An efficient discontinuous Galerkin finite element method for highly accurate solution of Maxwell equations," *IEEE Trans. Antennas Propag.*, vol. 60, no. 8, pp. 3992–3998, Aug. 2012.

[11] K. Sirenko, M. Liu, and H. Bagci, "Incorporation of exact boundary conditions into a discontinuous Galerkin finite element method for accurately solving 2D time-dependent Maxwell equations," *IEEE Trans. Antennas Propag.*, vol. 61, no. 1, pp. 472–477, Jan. 2013.

[12] P. Li, Y. Shi, L. J. Jiang, and H. Bagci, "A hybrid time-domain discontinuous Galerkin-boundary integral method for electromagnetic scattering analysis," *IEEE Trans. Antennas Propag.*, vol. 62, no. 5, pp. 2841–2846, May 2014.

[13] P. Li, Y. Shi, L. J. Jiang, and H. Bagci, "DGTD analysis of electromagnetic scattering from penetrable conductive objects with IBC," *IEEE Trans. Antennas Propag.*, vol. 63, no. 12, pp. 5686–5697, Dec. 2015.

[14] M. M. Botha, "Solving the volume integral equations of electromagnetic scattering," *J. Comput. Phys.*, vol. 218, no. 1, pp. 141–158, Oct. 2006.

[15] G. Kobidze and B. Shanker, "Integral equation based analysis of scattering from 3-D inhomogeneous anisotropic bodies," *IEEE Trans. Antennas Propag.*, vol. 52, no. 10, pp. 2650–2658, Oct. 2004.

[16] N. V. Budko and A. B. Samokhin, "Spectrum of the volume integral operator of electromagnetic scattering," *SIAM J. Sci. Comput.*, vol. 28, no. 2, pp. 682–700, Jan. 2006.

[17] J. Markkanen, C.-C. Lu, X. Cao, and P. Yla-Oijala, "Analysis of volume integral equation formulations for scattering by high-contrast penetrable objects," *IEEE Trans. Antennas Propag.*, vol. 60, no. 5, pp. 2367–2374, May 2012.

[18] J. Markkanen, "Discrete Helmholtz decomposition for electric current volume integral equation formulation," *IEEE Trans. Antennas Propag.*, vol. 62, no. 12, pp. 6282–6289, Dec. 2014.

[19] M. C. van Beurden and S. J. L. van Eijndhoven, "Well-posedness of domain integral equations for a dielectric object in homogeneous background," *J. Eng. Math.*, vol. 62, no. 3, pp. 289–302, Mar. 2008.

[20] J. Markkanen and P. Ylä-Oijala, "Numerical comparison of spectral properties of volume-integral-equation formulations," *J. Quant. Spectrosc. Radiati. Transf.*, vol. 178, pp. 269–275, Jul. 2016.

[21] J. Markkanen, P. Ylä-Oijala, and S. Järvenpää, "On the spectrum and preconditioning of electromagnetic volume integral equations," in *Proc. Int. Symp. Electromagn. Theory*, Espoo, Finland, Aug. 2016, pp. 834–835.

[22] J. Markkanen, "Numerical analysis of the potential formulation of the volume integral equation for electromagnetic scattering," *Radio Sci.*, vol. 52, no. 10, pp. 1301–1311, Oct. 2017.

[23] N. T. Gres, A. A. Ergin, B. Shanker, and E. Michielssen, "Volume-integral-equation-based analysis of transient electromagnetic scattering from three-dimensional inhomogeneous dielectric objects," *Radio Sci.*, vol. 36, no. 3, pp. 379–386, May/Jun. 2001.

[24] G. Kobidze, J. Gao, B. Shanker, and E. Michielssen, "A fast time domain integral equation based scheme for analyzing scattering from dispersive objects," *IEEE Trans. Antennas Propag.*, vol. 53, no. 3, pp. 1215–1226, Mar. 2005.

[25] B. Shanker, K. Aygün, and E. Michielssen, "Fast analysis of transient scattering from lossy inhomogeneous dielectric bodies," *Radio Sci.*, vol. 39, no. 2, pp. 1–14, Apr. 2004.

[26] S. B. Sayed, H. A. Ülkü, and H. Bagci, "A stable marching on-in-time scheme for solving the time-domain electric field volume integral equation on high-contrast scatterers," *IEEE Trans. Antennas Propag.*, vol. 63, no. 7, pp. 3098–3110, Jul. 2015.

[27] A. Al-Jarro, M. A. Salem, H. Bagci, T. M. Benson, P. Sewell, and A. Vukovic, "Explicit solution of the time domain volume integral equation using a stable predictor-corrector scheme," *IEEE Trans. Antennas Propag.*, vol. 60, no. 11, pp. 5203–5214, Nov. 2012.

[28] Y. Liu, A. Al-Jarro, H. Bagci, and E. Michielssen, "Parallel PWTD-accelerated explicit solution of the time-domain electric field volume integral equation," *IEEE Trans. Antennas Propag.*, vol. 64, no. 6, pp. 2378–2388, Jun. 2016.

[29] S. B. Sayed, H. A. Ulku, and H. Bagci, "An efficient explicit marching on in time solver for magnetic field volume integral equation," in *Proc. IEEE Int. Symp. Antennas Propag. Soc. (USNC/URSI)*, Vancouver, BC, Canada, Jul. 2015, pp. 1816–1817.

[30] J. Wang, M. Lu, and E. Michielssen, "A time-domain volume-integral equation approach for analyzing scattering from 2-D nonlinear objects under TM illumination," *Microw. Opt. Technol. Lett.*, vol. 26, no. 6, pp. 419–423, Sep. 2000.

[31] S. B. Sayed, H. A. Ulku, and H. Bagci, "An explicit MOT scheme for solving the TD-EFVIE on nonlinear and dispersive scatterers," in *Proc. IEEE Int. Symp. Antennas Propag. Soc. (USNC/URSI)*, San Diego, CA, USA, Jul. 2017, pp. 1135–1136.

[32] J.-M. Jin, *Theory and Computation of Electromagnetic Fields*. Hoboken, NJ, USA: Wiley, 2010.

[33] D. H. Schaubert, D. R. Wilton, and A. W. Glisson, "A tetrahedral modeling method for electromagnetic scattering by arbitrarily shaped inhomogeneous dielectric bodies," *IEEE Trans. Antennas Propag.*, vol. 32, no. 1, pp. 77–85, Jan. 1984.

[34] J.-C. Nédélec, "Mixed finite elements in $\mathbb{R}^3$," *Numer. Math.*, vol. 35, no. 3, pp. 315–341, 1980.

[35] J. P. Webb, "Hierarchal vector basis functions of arbitrary order for triangular and tetrahedral finite elements," *IEEE Trans. Antennas Propag.*, vol. 47, no. 8, pp. 1244–1253, Aug. 1999.

[36] A. F. Peterson, "Efficient solenoidal discretization of the volume EFIE for electromagnetic scattering from dielectric objects," *IEEE Trans. Antennas Propag.*, vol. 62, no. 3, pp. 1475–1478, Mar. 2014.

[37] H. A. Ulku, H. Bagci, and E. Michielssen, "Marching on-in-time solution of the time domain magnetic field integral equation using a predictor-corrector scheme," *IEEE Trans. Antennas Propag.*, vol. 61, no. 8, pp. 4120–4131, Aug. 2013.

[38] G. Manara, A. Monorchio, and R. Reggiannini, "A space-time discretization criterion for a stable time-marching solution of the electric field integral equation," *IEEE Trans. Antennas Propag.*, vol. 45, no. 3, pp. 527–532, Mar. 1997.

[39] K. Aygun, B. Shanker, A. A. Ergin, and E. Michielssen, "A two-level plane wave time-domain algorithm for fast analysis of EMC/EMI problems," *IEEE Trans. Electromagn. Compat.*, vol. 44, no. 1, pp. 152–164, Feb. 2002.

[40] H. Bagci, A. E. Yilmaz, V. Lomakin, and E. Michielssen, "Fast solution of mixed-potential time-domain integral equations for half-space environments," *IEEE Trans. Geosci. Remote Sens.*, vol. 43, no. 2, pp. 269–279, Feb. 2005.

[41] E. Hairer and G. Wanner, "Linear multistep method," *Scholarpedia*, vol. 5, no. 4, p. 4591, 2010.

[42] A. Glaser and V. Rokhlin, "A new class of highly accurate solvers for ordinary differential equations," *J. Sci. Comput.*, vol. 38, no. 3, pp. 368–399, Mar. 2009.

[43] E. H. S. Norsett and G. Wanner, *Solving Ordinary Differential Equations I: Nonstiff Problems*. New York, NY, USA: Springer-Verlag, 1987.

[44] A. Dutt, L. Greengard, and V. Rokhlin, "Spectral deferred correction methods for ordinary differential equations," *BIT Numer. Math.*, vol. 40, no. 2, pp. 241–266, Feb. 2000.

[45] P. J. Davis and P. Rabinowitz, *Methods of Numerical Integration*. Amsterdam, The Netherlands: Elsevier, 1984.

[46] D. J. Holdych, D. R. Noble, and R. B. Secor, "Quadrature rules for triangular and tetrahedral elements with generalized functions," *Int. J. Numer. Meth. Eng.*, vol. 73, no. 9, pp. 1310–1327, Feb. 2008.

[47] Y. Shi, H. Bagci, and M. Lu, "On the static loop modes in the marching-on-in-time solution of the time-domain electric field integral equation," *IEEE Antennas Wireless Propag. Lett.*, vol. 13, pp. 317–320, 2014.

[48] J. Knab, "Interpolation of band-limited functions using the approximate prolate series (Corresp.)," *IEEE Trans. Inf. Theory*, vol. IT-25, no. 6, pp. 717–720, Nov. 1979.

[49] R. A. Wildman, G. Pisharody, D. S. Weile, S. Balasubramaniam, and E. Michielssen, "An accurate scheme for the solution of the time-domain integral equations of electromagnetics using higher order vector bases and bandlimited extrapolation," *IEEE Trans. Antennas Propag.*, vol. 52, no. 11, pp. 2973–2984, Nov. 2004.

[50] A. E. Yilmaz, D. S. Weile, B. Shanker, J. Jin, and E. Michielssen, "Fast analysis of transient scattering in lossy media," *IEEE Antennas Wireless Propag. Lett.*, vol. 1, pp. 14–17, 2002.

[51] A. E. Yilmaz, J.-M. Jin, and E. Michielssen, "Time domain adaptive integral method for surface integral equations," *IEEE Trans. Antennas Propag.*, vol. 52, no. 10, pp. 2692–2708, Oct. 2004.

[52] A. E. Yılmaz, J.-M. Jin, and E. Michielssen, "A parallel FFT accelerated transient field-circuit simulator," *IEEE Trans. Microw. Theory Techn.*, vol. 53, no. 9, pp. 2851–2865, Sep. 2005.

[53] H. Bagci, A. E. Yilmaz, J.-M. Jin, and E. Michielssen, "Fast and rigorous analysis of EMC/EMI phenomena on electrically large and complex cable-loaded structures," *IEEE Trans. Electromagn. Compat.*, vol. 49, no. 2, pp. 361–381, May 2007.

[54] H. Bagci, A. E. Yilmaz, and E. Michielssen, "An FFT-accelerated time-domain multiconductor transmission line simulator," *IEEE Trans. Electromagn. Compat.*, vol. 52, no. 1, pp. 199–214, Feb. 2010.

[55] B. Shanker, A. A. Ergin, K. Aygun, and E. Michielssen, "Analysis of transient electromagnetic scattering phenomena using a two-level plane wave time-domain algorithm," *IEEE Trans. Antennas Propag.*, vol. 48, no. 4, pp. 510–523, Apr. 2000.

[56] B. Shanker, A. A. Ergin, M. Lu, and E. Michielssen, "Fast analysis of transient electromagnetic scattering phenomena using the multilevel plane wave time domain algorithm," *IEEE Trans. Antennas Propag.*, vol. 51, no. 3, pp. 628–641, Mar. 2003.

[57] A. E. Yilmaz, J. M. Jin, and E. Michielssen, "Analysis of low-frequency electromagnetic transients by an extended time-domain adaptive integral method," *IEEE Trans. Adv. Packag.*, vol. 30, no. 2, pp. 301–312, May 2007.

[58] R. W. Freund, "A transpose-free quasi-minimal residual algorithm for non-hermitian linear systems," *SIAM J. Sci. Stat. Comput.*, vol. 14, pp. 470–482, Mar. 1993.

Sadeed Bin Sayed (S'14–M'19) received the B.Tech. degree in electronics and communication engineering from the National Institute of Technology at Calicut, Kozhikode, India, in 2004, the M.Tech. degree in communications engineering from IIT Delhi, New Delhi, India, in 2007, and the Ph.D. degree from the King Abdullah University of Science and Technology (KAUST), Thuwal, Saudi Arabia, in 2018.

From July 2007 to May 2008, he was a member with Technical Staff Digibee Microsystems, Bengaluru, India. In May 2008, he joined as an Engineer with Qualcomm India Pvt. Ltd, Hyderabad, India. In 2019, he joined as a Research Fellow with the School of Electrical and Electronic Engineering, Nanyang Technological University, Singapore. His current research interests include the development of fast and accurate integral equations solvers and their application to real-life problems.

Dr. Sayed was a recipient of the Student Paper Finalist in 2016 and the Honorable Mention Award thrice in 2014, 2015, and 2017 at the IEEE International Symposiums on Antennas and Propagation (APS). He ranked third in the student paper competitions twice at the International Conference on Review of Progress in Applied Computational Electromagnetics (ACES), in 2014 and 2018.

Huseyin Arda Ulku (S'06–M'12–SM'19) received the B.S., M.S., and Ph.D. degrees in electronics engineering from Gebze Technical University (GTU) (formerly Gebze Institute of Technology), Kocaeli, Turkey, in 2006, 2008, and 2011, respectively.

From 2007 to 2011, he was a Research and Teaching Assistant with the Electromagnetic Fields and Microwave Division, Department of Electronics Engineering, GTU. From 2011 to 2015, he was a Post-Doctoral Fellow with the Division of Computer, Electrical, and Mathematical Science and Engineering (CEMSE), King Abdullah University of Science and Technology (KAUST), Thuwal, Saudi Arabia. Since 2015, he has been with GTU, where he is currently an Associate Professor of electrical engineering. His current research interests include computational electromagnetics with a focus on time domain integral equations.

Dr. Ulku's graduate studies were partially supported by the Scientific and Technical Research Council of Turkey (TUBITAK). In 2009, he received the Leopold B. Felsen Award for Excellence in Electromagnetics (selected from Turkish students/researchers in the field of electromagnetics) funded by the Leopold B. Felsen Fund and Dogus University.

Hakan Bagci (S'97–M'07–SM'14) received the B.S. degree in electrical and electronics engineering from Bilkent University, Ankara, Turkey, in 2001, and the M.S. and Ph.D. degrees in electrical and computer engineering from the University of Illinois at Urbana–Champaign (UIUC), Urbana, IL, USA, in 2003 and 2007, respectively.

From June 1999 to July 2001, he was as an Undergraduate Researcher with the Computational Electromagnetics Group, Bilkent University. From August 2001 to December 2006, he was a Research Assistant with the Center for Computational Electromagnetics and Electromagnetics Laboratory, UIUC. From January 2007 to August 2009, he was a Research Fellow with the Radiation Laboratory, University of Michigan, Ann Arbor, MI, USA. Since August 2009, he has been with the King Abdullah University of Science and Technology (KAUST), Thuwal, Saudi Arabia, where he is currently an Associate Professor of electrical engineering. He has authored or coauthored more than 90 journal articles and more than 200 articles in conference proceedings. His current research interests include various aspects of theoretical and applied computational electromagnetics with emphasis on well-conditioned frequency and time-domain integral equation formulations and their discretization, hybrid time-domain integral and differential equation solvers, accurate, stable, and efficient marching schemes for time-domain solvers, stochastic characterization of electromagnetic field and wave interactions on complex geometries, and solution of 2-D and 3-D electromagnetic inverse scattering problem using signal processing techniques.

Dr. Bagci was a recipient of the 2008 International Union of Radio Scientists (URSI) Young Scientist Award and the 2004–2005 Interdisciplinary Graduate Fellowship from the Computational Science and Engineering Department, UIUC. His article titled "Fast and Rigorous Analysis of EMC/EMI Phenomena on Electrically Large and Complex Structures Loaded With Coaxial Cables" was one of the three finalists (with honorable mention) for the 2008 Richard B. Schulz Best Transactions Paper Award given by the IEEE Electromagnetic Compatibility Society. He has authored (as student) or coauthored (as student and advisor) 17 finalist/honorable mention papers in the student paper competitions at the 2005, 2008, 2010, 2014, 2015, 2016, 2017, and 2018 IEEE Antennas and Propagation Society International Symposiums and the 2013, 2014, 2016, 2017, and 2018 Applied Computational Electromagnetics Society Conferences. He is currently an Associate Editor of the IEEE TRANSACTIONS ON ANTENNAS AND PROPAGATION, the IEEE JOURNAL ON MULTISCALE AND MULTIPHYSICS COMPUTATIONAL TECHNIQUES, and the *IEEE Antennas and Propagation Magazine*.